Application of Spatial Features to Classification, Segmentation and Sharpening in Remotely Sensed Images

（リモートセンシング画像の分類、分割、鮮鋭化への空間特徴の適用）

CHEN, Xuehong

(陳 学泓)

Application of Spatial Features to Classification, Segmentation and Sharpening in Remotely Sensed Images

（リモートセンシング画像の分類、分割、鮮鋭化への空間特徴の適用）

CHEN, Xuehong

(陳 学泓)

A dissertation for the degree of Doctor of Science

Department of Earth and Environmental Sciences,

Graduate School of Environmental Studies, Nagoya University

(名古屋大学大学院環境学研究科地球環境科学専攻学位論文　博士　(理学))

2012

CONTENTS

List of Figures

List of Tables

SUMMARY

The capability of acquiring continuous surface data is one of the most important superiorities of remote sensing compared with conventional field investigation. Because the spatial distributions of the geographic elements are not independent, many spatial features (such as landscape pattern, contextual information, spatial autocorrelation, etc.) can be shown in the remotely sensed images. Till now, a number of mathematical tools have been developed to describe the spatial features from different aspects, which can be categorized into three types depending on their calculating approaches: moving-window based, object based, and image based methods. Although these methods were widely applied in remote sensing, they were simply used without much consideration of the particular geographic characteristics and their applications were limited on land cover classification or change detection. Therefore, this thesis attempts to extend the application of spatial features in the following fields:

(1) A moving-window based method was applied in the field of classification accuracy assessment. For the landscape analysis, classification error in a land cover map will be propagated into the calculation of the landscape patter indices. However, the traditional classification accuracy indices consider only the amount of classification error without their spatial distribution, consequently cannot well

predict the error of landscape pattern indices induced by classification error. Therefore, in chapter 2, a new measure of classification error, Weighted Misclassification Rate, which is based on the moving-window technique, was proposed to predict the error of landscape pattern indices induced by classification error.

(2) A moving-window based method, Markov Random Fields model, was employed in an automated land cover updating approach. Although many classification techniques were intensively studied, there is a lack of a totally automated approach for updating land cover maps. In chapter 3, the author proposed an automated updating approach which integrates the change detection technique, Markov Random Fields model, and an iterated training sample selecting procedure, to produce reasonable land cover maps efficiently.

(3) Uncertainties in object based methods were quantified. Although object based methods were intensively studied, the uncertainties in image segmentation were largely neglected in the previous studies. In chapter 4, a new soft segmentation model was developed for quantitatively describing the uncertainties in the segmented results.

(4) An Image based method was used for investigating the scale effect of the relationship between vegetation index and surface temperature. Such relationship was used for improving the spatial resolution of thermal infrared images because the visual-near infrared images are usually with higher spatial resolution.

However, the scale effect of this relationship was neglected in the previous studies. In chapter 5, the scale effect was investigated and a more robust spatial sharpening method for thermal imagery was proposed.

CHAPTER 1

Introduction

1.1 Background

Remote sensing is commonly defined as the science (and to some extent, art) of obtaining and analyzing the information about the earth surface from the distant sensor in the airplane or satellite (Lillesand and Kiefer, 2000). In general, remotely sensed data are recorded as the 2-dimension images with spectral bands information on different dates (Fig. 1.1). Therefore, remotely sensed images include three dimensions of information: i) spatial information; ii) spectral information; iii) temporal information. And the quality of remote sensing data depends on its spatial, spectral, and temporal resolutions (revisit time of the satellite).

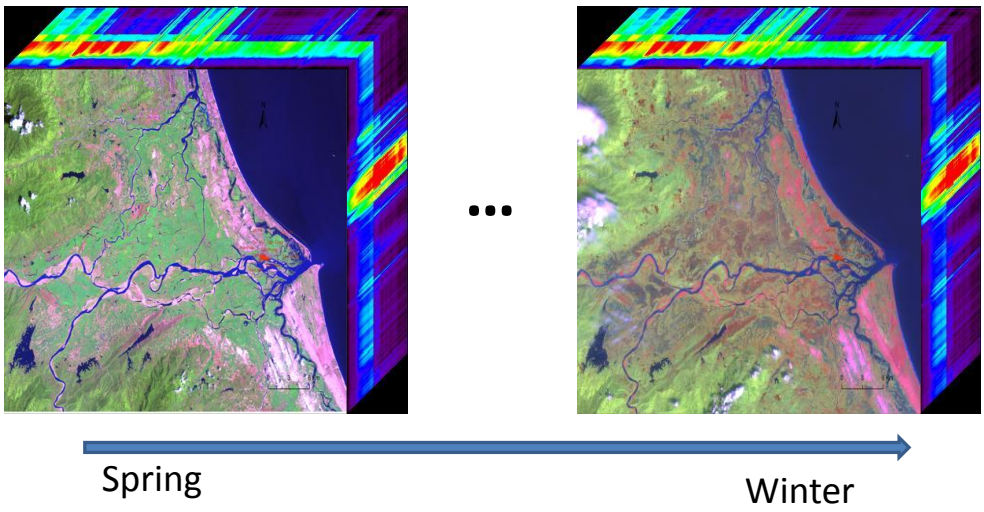

Fig. 1.1 Three dimensions of information (spatial, spectral, and temporal information) in remotely sensed images

Till now, algorithms and applications have been intensively studied for mining the spectral information and temporal information of satellite images. Spectral information has been used for land cover mapping (e.g. Richard and Jia, 2006), quantitatively retrieving of biophysical parameters (e.g. Liang, 2004), and so on. Temporal information has been applied in land cover change detection (e.g. Lu et al., 2004), phenology study (e.g. Zhang et al., 2003), disaster monitoring (e.g. Tralli et al., 2005), and so on. Many technologies used for extracting the spectral and temporal information were developed by the remote sensing community and show a very particular geophysical or biophysical characteristic. A representative example is the development of vegetation indices which considers the particular spectral response of vegetation, atmospheric effect and other factors (Bannari et al., 1995).

In contrast, although more and more attentions have been paid on the spatial information mining since the appeal of Blaschke and Strobl (2001), most of the studies simply used the mathematical tools of digital image processing without much consideration of the particular geographic characteristics, and the applications were limited on land cover classification or change detection. Therefore, there is a great potential of improving the mathematical tools of spatial feature extraction by considering more geographic characteristics or applying them in more research fields rather than classification.

The introduction part is organized as follows. In section 1.2, a brief review of the studies on spatial feature extraction in remote sensing is presented. In section 1.3, the

author introduces several gaps in the previous studies and presented the framework of this doctor thesis.

1.2 Review of the Studies on the Spatial Feature Extraction

There is no strict definition of the spatial feature. It usually includes landscape pattern, texture, spatial autocorrelation, and other features related with spatial distribution. Because of its complexity, there is not a uniform spatial feature description method which is commonly accepted. Till now, many mathematical tools have been developed to describe the spatial feature from different aspects. In this review, we categorized them into three types depending on the calculating methods: moving-window based, object based, and image based methods.

1.2.1 Moving-Window Based Methods

The moving-window is the most commonly used tool for extracting the spatial features in the images. The methods based on moving-window include spatial domain filter, Markov Random Field Model, Mathematical Morphology and Co-occurrence matrix.

(1) Spatial domain filter

In this method, a moving window is established that contains an array of coefficients or weighting factors. Such arrays are referred to as operators or kernels. Then, the kernel is moved throughout the original image, and the value at the center

of the kernel in the filtered image is obtained by multiplying each coefficient in the kernel by the corresponding DN (Digital Number) in the original image and adding all the result products. Depending on the different kernels, the spatial domain filters can be applied for smoothing images, sharpening images, enhancing edges and so on (Lillesand and Kiefer, 2000).

(2) Markov Random Field Model

Markov Random Field (MRF) is a probabilistic process in which all interaction is local; the probability that a cell is in a given state is entirely determined by probability states of neighboring cells (Materka and Strzelecki, 1998). It has been used for improving classification and change detection result by reducing the “salt and pepper” error in pixel based classification or change detection methods (Bruzzone and Prieto, 2000).

(3) Mathematical Morphology

The basic idea in binary morphology is to probe an image with a simple, pre-defined shape, drawing conclusions on how this shape fits or misses the shapes in the image (Comer and Delp, 1999). This simple "probe" is called structuring element, and is itself a binary image (e.g., a subset of the space or grid). The basic operations of mathematical morphology include erosion, dilation, open and close. Mathematical morphology has been used for classification, endmember extraction, speckle removal on radar data, etc. (Soille and Pesaresi, 2002, Plaza et al., 2002).

(4) Co-occurrence matrix

The co-occurrence-matrix describes second-order statistic of texture, which is a matrix of estimated probabilities of transitions from level r_1 to level r_2 for given vector **v**, and vector **v** defines direction of construction of the matrix and distance between points that have intensities r_1 and r_2 (Materka and Strzelecki, 1998). The co-occurrence-matrix was widely applied in extracting the textural information of remotely sensed images.

In summary, moving-window based methods are easy to conduct and with high computing efficiency, therefore have been widely applied in the previous studies.

1.2.2 Object Based Methods

Object based image analysis methods receive more and more attentions in remote sensing community (Blaschke, 2010). The first step of object based image analysis is segmentation which produces a set of non-overlapping objects (polygons, patches). The segmentation algorithm can be mainly categorized into image driven based, model driven based, and homogeneity measure based methods (Dey et al., 2010). Now, commercial softwares eCognition and ENVI EX are also available for image segmentation, which stimulates related studies. The second step is the analysis for the segmented image. Most applications focused on land cover/land use classification and change detection. Only a few studies focused on quantitative retrieving of biophysical parameter (e.g. Addink et al., 2007). Object based method is promising for extracting spatial feature of the images, especially for the images with high spatial resolution;

however, it requires high computation cost and many parameters which are usually difficult to determine suitably.

1.2.3 Image Based Methods

Image based methods include global spatial autocorrelation index, semivariogram, Fourier transformation and so on. They describe the overall features of the spatial pattern. Although without spatial explicit information, this kind of methods are still widely applied in many studies. For example, the semivariogram is usually applied for studying the scale effect of the images (e.g. Woodcock and Strahler, 1987, Román et al., 2009). Fourier transformation could be used for removing the stripe noise in remotely sensed images (Chen et al., 2004).

1.3 Contents of this Thesis

Although the spatial features of remotely sensed images have already received much attention, there are still many gaps in the previous studies. This thesis found and filled some gaps in the previous studies.

(1) Weighted Misclassification Rate (WMR)

Moving-window based methods have been applied in classification, however, was never considered in the classification accuracy assessment. Especially for the landscape analysis, classification error will be propagated into the calculation of landscape patter index, while the traditional classification accuracy index cannot

reflect such error correctly. Therefore, in chapter 2, the author proposed a new measure of classification error, Weighted Misclassification Rate (WMR), based on the moving-window technique. WMR considers the spatial distribution of classification error, and can well predict the error of landscape pattern index (LPI).

(2) An integrated, automated approach for updating land cover maps

Although classification techniques were intensively studied, there is a lack of a totally automated approach for updating land cover maps. In chapter 3, we developed an automated approach which integrates the change detection technique, Markov Random Fields model, and an iterated training sample selecting procedure. The new approach can update land cover maps with reasonable accuracy efficiently.

(3) Soft segmentation model

There are always uncertainties or errors in image segmentation. Unfortunately such uncertainty information was rarely considered in the previous studies. In chapter 4, a soft segmentation model was developed for quantitatively describing the uncertainties in the segmented result.

(4) Scale effect of the relationship between vegetation index and surface temperature

Image based methods were usually used for processing the gray images, while were rarely applied in the multi-band images. In chapter 5, the author investigated the scale effect of the relationship between vegetation index and surface temperature

using the image based method. Based on the investigated result, a more robust thermal sharpening method was proposed.

The framework of this thesis is shown in Fig. 1.2.

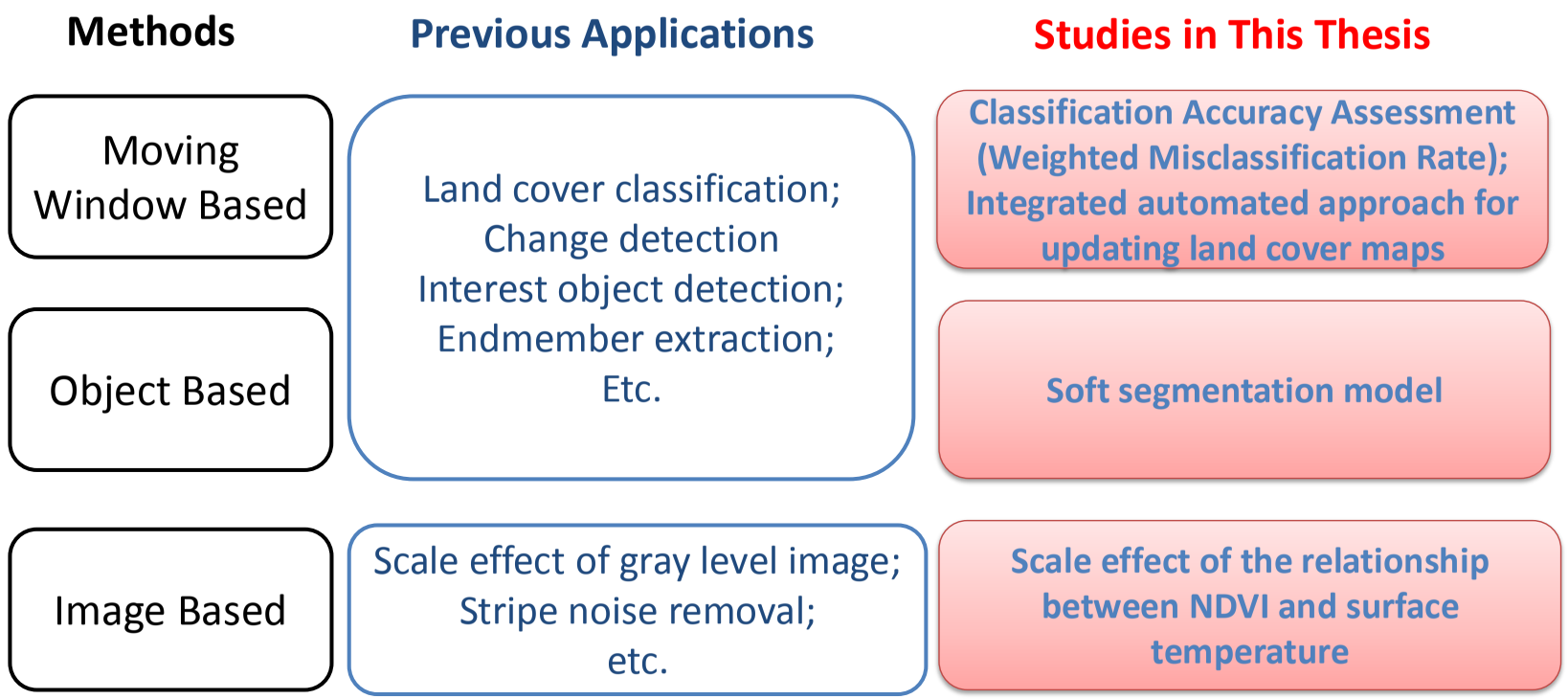

Fig. 1.2 Framework of this thesis

CHAPTER 2

Weighted Misclassification Rate: A New Measure of Classification Error Designed for Landscape Pattern Index

2.1 Introduction

As one of the most important topics in landscape ecology, a large number of landscape pattern index (LPI) have been developed to quantitatively describe the landscape pattern (Turner, 2005). Moreover, an excellent software package, Fragstats (McGarigal and Marks, 2002), which stimulates the broad application of LPI in various fields, is also available for calculating LPIs.

Remotely sensed data have been widely used to derive LPIs (Newton et al., 2009). Unfortunately, inevitable misclassification in classified thematic maps have not attracted adequate attention in LPI-related literature (e.g. Shao and Wu, 2008), although misclassification errors can propagate into LPI calculation, as reported by Hess (1994). Until now, due to the unstable relationship between classification accuracy assessment indices and the LPI error (Langford et al., 2006), which is defined as the difference between the LPIs calculated from reference map (ground truth) and the LPIs calculated from the classified map with error, few studies have examined the impact of classification errors on the calculation of LPI (Shao and Wu, 2008). Generally, the overall accuracy (OA) and kappa coefficient (κ) derived from the confusion matrix are the most popular indices for assessing classification error in

the remote sensing community (Foody, 2002). However, such indices focus on only the amount of misclassified pixels, without considering the spatial distribution of the pixels, whereas the reliability of LPI calculation as a measure of spatial heterogeneity depends primarily on the spatial pattern of classification errors. Consequently, they are not suitable for estimating the LPI error that arises from classification. Therefore, a new measure of classification error that can provide a reliable indicator of LPI error is needed. One possible solution is to develop an object-based assessment method (e.g., Zhan et al., 2009). However, this is not practicable for remotely sensed images, because obtaining the reference ground truth for the entire region of interest would be too expensive and difficult (Stehman, 2009). Accuracy assessment based on multi-resolution comparison is also a promising method (Kuzera and Pontius, 2008; Pontius and Connors, 2009). However, as an effective method that directly reflects LPI error, such assessment still requires improvement and further validation.

Therefore, in order to provide a new measure of classification error that can provide a reliable indicator of LPI error, we propose a new classification accuracy assessment index referred to as the Weighted Misclassification Rate (WMR), which, although pixel-based, integrates the spatial distribution information of misclassified pixels by considering the adjacent pixels. A series of simulated images were used to test the performance of the newly proposed WMR.

2.2 New Measure of Classification Error

2.2.1 Weighted Misclassification Rate Development

An ideal classification error measure designed for LPI calculation should satisfy two requirements: 1) high correlation with LPI error and 2) convenience of sampling. Since misclassified pixels located at different positions may affect the landscape pattern and have a further effect on LPI error to different degree, we proposed a Weighted Misclassification Rate (WMR) by assigning different weights to different sampled pixels:

$$\mathrm{WMR} = \frac{\sum_{i=1}^{N} w_i}{N} \times 100\% \tag{2-1}$$

where N is the number of all sampled pixels and w_i is the weight of one sampled pixel i. Since edge length and connectivity are two important aspects of the landscape pattern, a misclassified pixel that affects edge length and connectivity of a patch should be assigned a larger weight. Since WMR is calculated at the pixel level, we defined the edge number, which is an indicator of edge length at the pixel level, as the number of four-neighborhood pixels belonging to different classes than pixel i. Here, only four-neighborhood pixels are used because the total edge is calculated based on four-neighborhood pixels in Fragstats. In addition, the isolation of pixel i, which reflects patch connectivity, is defined based on whether there is at least one pixel belonging to the same class as pixel i around eight-neighborhood pixels. If there is no pixel belonging to the same class as pixel i around the eight neighborhood pixels, then the isolation of pixel i is given as 1, indicating that the target pixel i is completely isolated. Otherwise, it is given as zero. The weight of pixel i is thus calculated based

on the reference and classification data in 3×3 windows according to the changes in edge number and isolation of the pixel resulting from misclassification:

$$w_i = \frac{1}{2}\left[\frac{(p_{ci} - p_{ri})}{4} + (q_{ci} - q_{ri})\right] \quad (2\text{-}2)$$

where p_{ci} and p_{ri} are the edge number of pixel i in the classification map awaiting assessment and in the reference map, respectively. The term (p_{ci} - p_{ri})/4 ranges from -1 to 1, reflecting the change in the edge number due to misclassification. The terms q_{ci} and q_{ri} are the isolation of pixel i in the classification map and in the reference map, respectively. The term of (q_{ci} - q_{ri}) has three distinct values, -1, 0, and 1, that specify the isolation change of the pixel due to misclassification. A positive value of w_i indicates that pixel misclassification enhances the fragmentation of the map relative to the reference map, whereas a negative value of w_i indicates that pixel misclassification reduces the fragmentation of the map relative to the reference map. If the sampled pixels in the 3×3 windows are correctly classified, the edge number and the isolation of the central pixel keeps unchanged, and the weight is equal to zero.

Fig. 2.1 shows examples of the weight calculation. From Case (a) to Case (e), the weight changes from -1 to 1, reflecting the degree to which the landscape fragmentation is affected by the misclassified pixel, according to its spatial configuration. WMR can also be calculated on the class level after minor modification. First, a multi-class map is converted into a two-class map, in which one class is the target class and the other class, which is made up of the remaining classes, is the background class. Then, WMR can be calculated based on the two-class map.

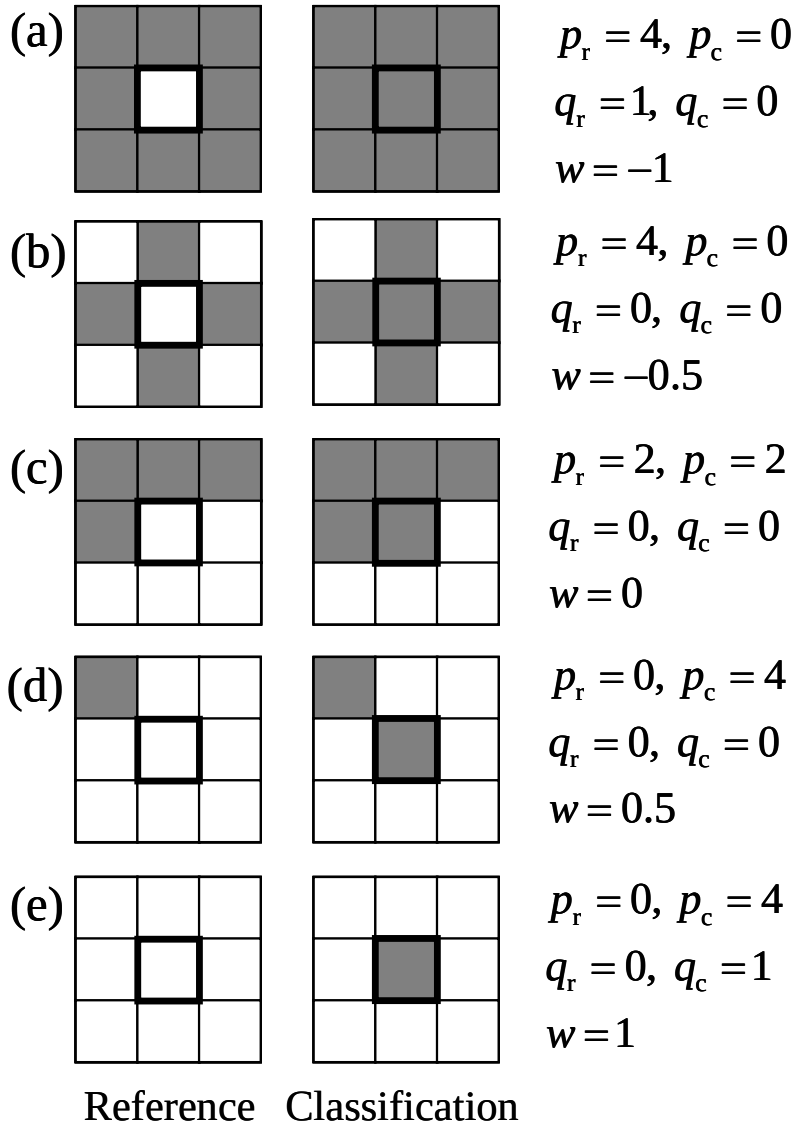

Fig. 2.1 Illustration of weight calculation (a. w = -1; b. w = -0.5; c. w = 0; d. w = 0.5; e. w = 1)

2.2.2 Statistical Properties of WMR

Since WMR is the mean estimate of w_i, we derived the expected value and variance of the mean estimate using different sampling methods. The expected value and variance of w_i are denoted as E(w) and Var(w), respectively.

Under the random sampling method, the expected value and variance of the mean estimate are E(w) and Var(w)/N, respectively, where N is the sample size. The mean estimate is unbiased, and the variance decreases with the increase in the sample size.

Under the proportionally allocated stratified random sampling method, the pixels are divided into m strata, where m is the number of classes. Here, w_i of each stratum is denoted as X_k, k = 1, …, m, and the proportions of each stratum is denoted as f_k, k = 1, ..., m. Then, the expected value of the mean estimate is $\sum_{k=1}^{m} f_k \, \mathrm{E}(X_k)$, which is equal to E($w$), and so is unbiased. The variance of the mean estimate is $\sum_{k=1}^{m} f_k \, \mathrm{Var}(X_k) / N$. According to the law of total variance, Var(w) can be described as:

$$\mathrm{Var}(w) = \sum_{k=1}^{m} f_k \, \mathrm{Var}(X_k) + \mathrm{Var}\left(\mathrm{E}(X_k)\right). \tag{2-3}$$

Therefore, the variance of the mean estimate under the proportional allocated stratified random sampling method is less than that under the random sampling method, especially when the term of $\mathrm{Var}\left(\mathrm{E}(X_k)\right)$ is large, which means that the error rate in various classes is largely different.

Under the stratified sampling method with each stratum having the same sample size, the expected value of the mean estimate is equal to $\sum_{k=1}^{m} \mathrm{E}(X_k)$, which is biased. Therefore, such a sampling method is not appropriate for WMR calculation.

2.3. Simulation Study

2.3.1 Data Simulation

In the present study, instead of using actual reference and classification maps, a series of reference and classification maps were simulated because it is difficult to obtain the ground truth of a large number of actual classification maps for analysis, whereas for simulated data, the completed reference data can be acquired easily, and the classification error can be controlled to the desired range (Chen et al., 2010). The Simmap (Saura and Martinez-Millan, 2000) map simulation software package was used to generate a total of 75 correct base maps (reference maps) to represent the various landscapes without classification error (see, for example, Fig. 2.2). The size of the map is 200 pixels × 200 pixels, and the number of classes is three. In Simmap, fragmentation of the landscapes is determined by the degree of aggregation, which is controlled by the parameter called as initial probability (*P*). As *P* increases, the number of patches decreases, and the mean and maximum size of the patches increase, resulting in increasingly aggregated landscapes (Saura and Martinez-Millan, 2000). We varied the class proportions and aggregation level and used the following five proportion configurations:

$$\begin{aligned} &f_1 = 0.125,\ f_2 = 0.125,\ f_3 = 0.750 \\ &f_1 = 0.125,\ f_2 = 0.250,\ f_3 = 0.625 \\ &f_1 = 0.125,\ f_2 = 0.375,\ f_3 = 0.500 \\ &f_1 = 0.250,\ f_2 = 0.250,\ f_3 = 0.500 \\ &f_1 = 0.333,\ f_2 = 0.333,\ f_3 = 0.333 \end{aligned} \tag{2-4}$$

where f_1, f_2, and f_3 denote the proportions of three classes. Three levels of aggregation (P = 0.1, 0.3, and 0.5), were considered. Five maps were generated for each combination of proportion and aggregation configuration.

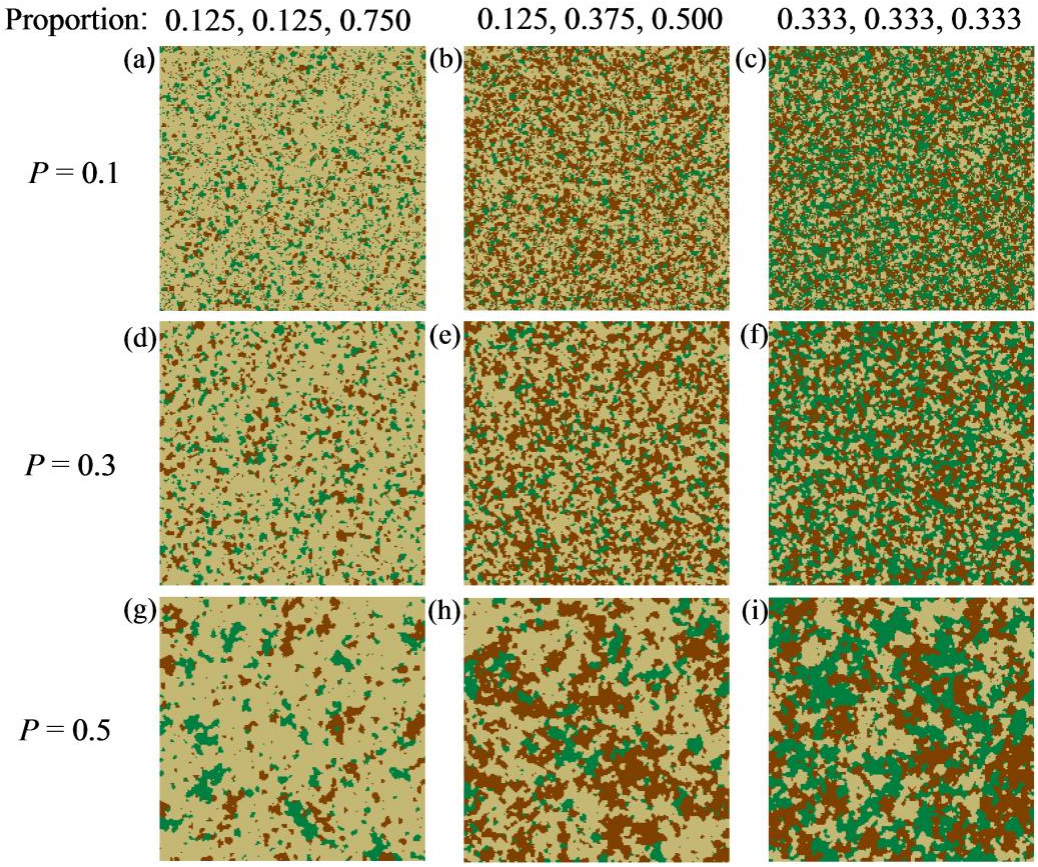

Fig. 2.2 Examples of simulated reference classification maps with a range of proportion and aggregation configurations (a. P = 0.1, f_1 = 0.125, f_2 = 0.125, f_3 = 0.750; b. P = 0.1, f_1 = 0.125, f_2 = 0.375, f_3 = 0.500; c. P = 0.1, f_1 = 0.333, f_2 = 0.333, f_3 = 0.333; d. P = 0.3, f_1 = 0.125, f_2 = 0.125, f_3 = 0.750; e. P = 0.3, f_1 = 0.125, f_2 = 0.375, f_3 = 0.500; f. P = 0.3, f_1 = 0.333, f_2 = 0.333, f_3 = 0.333; g. P = 0.5, f_1 = 0.125, f_2 = 0.125, f_3 = 0.750; h. P = 0.5, f_1 = 0.125, f_2 = 0.375, f_3 = 0.500; i. P = 0.5, f_1 = 0.333, f_2 = 0.333, f_3 = 0.333)

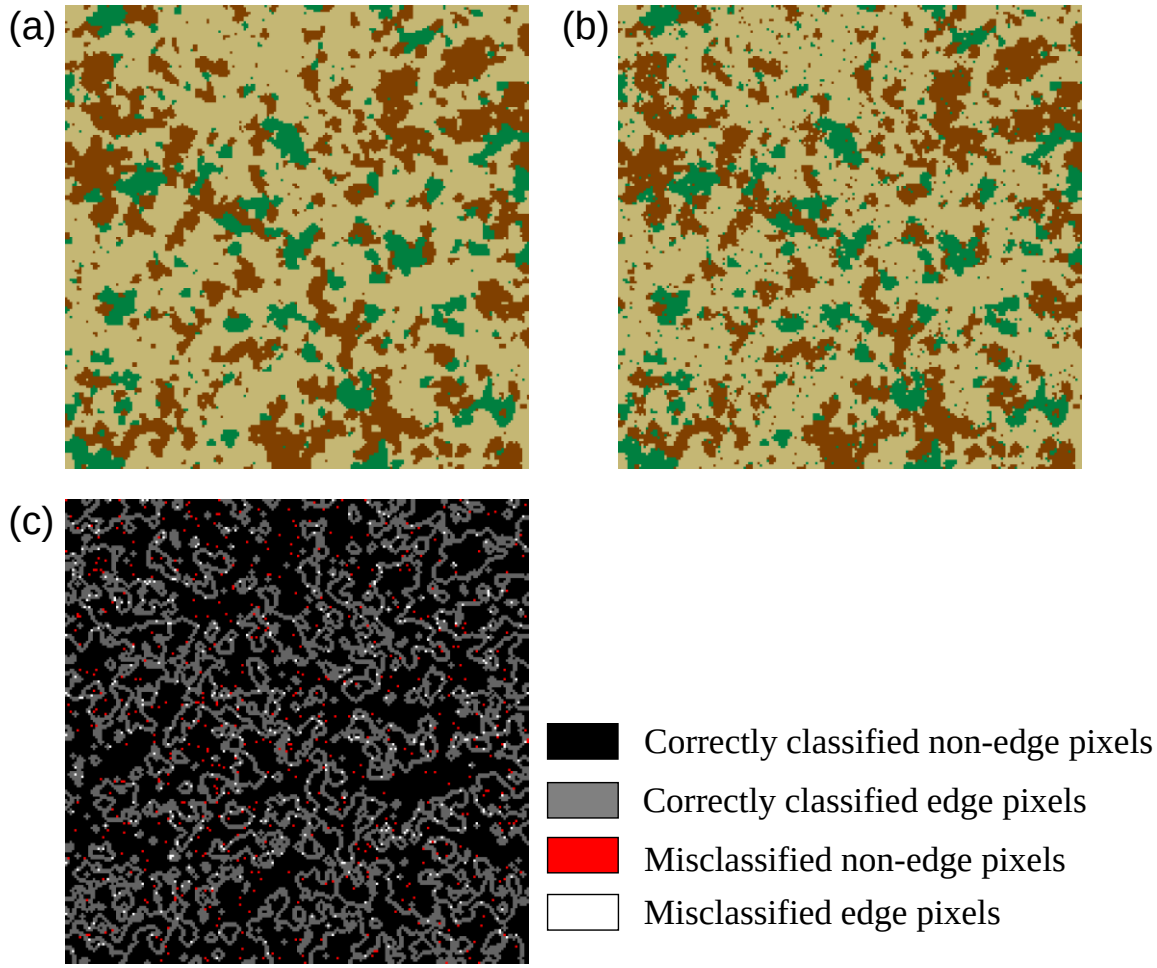

Fig. 2.3 Illustration of the simulated classification error (a. reference classification map; b. classification map with error; c. spatial distribution of the simulated misclassification pixels)

We simulated the classification maps by changing the classes of some pixels to the other two classes in the reference maps in order to represent misclassification by a classifier (Fig. 2.3). Regarding the spatial distribution of classification error, the misclassification probability of edge pixels was set as two times that of non-edge pixels (Fig. 2.3c), because mixed pixels in the border often lead to increased

classification error due to spectral mixture. For each reference map, we simulated five misclassification maps, in which the misclassified pixels covered 4% and 2%, 8% and 4%, 12% and 6%, 16% and 8%, and 20% and 10% of edge and non-edge pixels, respectively. In summary, a total of 375 (= 75 × 5) incorrect classification maps were simulated.

2.3.2 Measuring Fragmentation and LPI Error

We used FRAGSTATS 3.0 (McGarigal et al., 2002) to calculate the LPIs. Based on the recommendation of Li et al. (2005), six important LPI indices were calculated: (a) Number of Patches (NP), (b) Mean Patch Size (MPS), (c) Total Edge (TE), (d) Double-Logged Fractal Dimension (DLFD), (e) Contagion (CONTAG), and (f) Aggregation Index (AI). All of these indices were calculated on the landscape level and the class level, except for CONTAG, which is available only for the landscape level. For each LPI both on the landscape level and the class level, the LPI error is calculated as followed:

$$\mathrm{LPI}_{\mathrm{error}} = (\mathrm{LPI})_{\mathrm{reference}} - (\mathrm{LPI})_{\mathrm{classification}} \qquad (2\text{-}5)$$

where $\mathrm{LPI}_{\mathrm{reference}}$ is the LPI of the reference map and $\mathrm{LPI}_{\mathrm{classification}}$ is the LPI of the classification map.

2.3.3 Measuring the Classification Error

Overall accuracy, kappa coefficient, and the proposed WMR were used to measure the classification error. The accuracy indices were calculated based on all pixels of one map (40,000 pixels) to remove the sample effect. Two levels of accuracy assessment indices, which correspond to the landscape level and the class level of LPIs, respectively, were calculated.

2.3.4 Analysis of Results

Based on the 375 simulated classification maps, we investigated the correlation between LPI error and the accuracy assessment indices on both the landscape level and class level. For the class level, we chose only one class to analyze because there are no differences among three classes. Additionally, we also investigated the correlation between LPI error and the accuracy assessment indices on the landscape level under different subsets of simulation data.

Sample size is an important factor in assessment of classification error. The effect of sample size was also examined for the new index. For each simulated classification map, WMR were calculated based on different sample sizes, ranging from 400 to 4000 with an interval of 400. Here, we used proportional stratified random sampling method and randomly sample 500 times for each level of sample size. For each sample size, Root Mean Square Error (RMSE) of estimated WMR was calculated as followed:

$$\mathrm{RMSE} = \sqrt{\frac{\sum_{i=1}^{375}\sum_{j=1}^{500}(\mathrm{WMR}_{i,j} - \mathrm{WMR}_{i,\ \mathrm{full\_sample}})^2}{375 \times 500}} \tag{2-6}$$

where $\mathrm{WMR}_{i,j}$ is the WMR calculated from the *j*th sample of the *i*th simulated classification map, $\mathrm{WMR}_{i,\ \mathrm{full\_sample}}$ is the WMR calculated from full sample of the *i*th simulated classification map, which is regarded as the true value of WMR. RMSE indicates the accuracy of the estimated WMR. Then, the relationship between RMSE and sample size was investigated.

2.4 Results

2.4.1 Correlation between LPI error and classification accuracy indices

In the correlation analysis between LPI error and classification accuracy indices, we used the fully sampling method to remove the effect of sample size. Tables 2.1 and 2.2 show the correlation coefficients between the LPI error and the classification accuracy assessment indices, respectively, on the landscape level and the class level. WMR is better correlated with LPI error than overall accuracy and kappa coefficient in all cases, especially for the cases of NP, TE, CONTAG, AI, and DLFD. Among these LPI indices, the correlation coefficient between the error of MPS and WMR is decreased substantially. Although MPS is not particularly correlated with other LPIs, the correlations between the MPS error and the error of other LPIs are particularly low (results are not presented in the tables). That is because the MPS error is very sensitive to the true value of MPS, while the true value is unknown. For example, one

isolated misclassified pixel increases the NP by 1 and the TE by 4, regardless of the true values of NP and TE. However, the degree to which one isolated misclassified pixel decrease MPS depends on the true value of MPS.

Table 2.1 Correlation coefficients between classification accuracy assessment indices and LPI error on landscape level (n = 375)

Accuracy Index	NP	TE	MPS	CONTAG	AI	DLFD
	Correlation Coefficients					
OA	-0.575	-0.801	0.027	-0.516	-0.801	-0.739
κ	-0.659	-0.840	-0.077	-0.691	-0.839	-0.876
WMR	0.983	0.987	0.580	0.944	0.987	0.917

Table 2.2 Correlation coefficients between classification accuracy assessment indices and LPI error on class level (n = 375)

Accuracy Index	NP	TE	MPS	AI	DLFD
	Correlation Coefficients				
OA	-0.437	-0.816	0.048	-0.442	-0.649
κ	-0.768	-0.878	-0.139	-0.708	-0.937
WMR	0.934	0.978	0.315	0.895	0.939

Tables 2.3 and 2.4 show the correlation coefficients between the LPI error and the classification accuracy assessment indices on the landscape level under different subsets of simulation data. Strong correlations between WMR and LPI error (except for MPS) are observed for all subsets. For subsets of different aggregation levels (Table 2.3), the kappa coefficient is also well correlated with the LPI error. However,

for the subsets of different proportion configurations (Table 2.4), only WMR is well correlated with LPI error (except for MPS). Since LPIs are usually compared among the landscapes with different aggregation levels, WMR is more meaningful than kappa coefficient. The results for the class level are similar and so are not presented.

Table 2.3 Correlation coefficients between classification accuracy assessment indices and LPI error on landscape level under different aggregation levels (n = 125)

Aggregation level	Accuracy Index	NP	TE	MPS	CONTAG	AI	DLFD
		Correlation Coefficients					
P = 0.1	OA	-0.749	-0.903	-0.639	-0.555	-0.904	-0.729
	κ	-0.907	-0.993	-0.765	-0.795	-0.993	-0.908
	WMR	0.973	0.990	0.842	0.910	0.990	0.953
P = 0.3	OA	-0.908	-0.971	-0.647	-0.748	-0.972	-0.846
	κ	-0.991	-0.988	-0.823	-0.933	-0.989	-0.972
	WMR	0.996	0.993	0.838	0.927	0.993	0.958
P = 0.5	OA	-0.970	-0.989	-0.458	-0.875	-0.989	-0.943
	κ	-0.976	-0.957	-0.748	-0.990	-0.957	-0.983
	WMR	0.999	0.997	0.619	0.954	0.997	0.985

2.4.2 Effect of sample size

Fig. 2.4 shows the RMSE of WMR against sample size on the landscape level and class level. It can be seen that the RMSE of new index decrease when the sample size increases. This result is consistent with other studies on the sample effect of the accuracy indices of hard and soft classification (Stehman, 1996; Chen et al., 2010).

Table 2.4 Correlation coefficients between classification accuracy assessment indices and LPI error on landscape level under different proportion configurations (n = 75)

Proportion Configuration	Accuracy Index	NP	TE	MPS	CONTAG	AI	DLFD
		Correlation Coefficients					
f_1 = 0.125	OA	-0.748	-0.917	0.029	-0.823	-0.916	-0.960
f_2 = 0.125	κ	-0.799	-0.945	-0.051	-0.869	-0.945	-0.977
f_3 = 0.750	WMR	0.980	0.991	0.432	0.994	0.991	0.930
f_1 = 0.125	OA	-0.651	-0.856	0.024	-0.714	-0.855	-0.873
f_2 = 0.250	κ	-0.666	-0.866	0.008	-0.728	-0.865	-0.881
f_3 = 0.625	WMR	0.981	0.990	0.554	0.991	0.990	0.957
f_1 = 0.125	OA	-0.678	-0.822	0.008	-0.648	-0.821	-0.788
f_2 = 0.375	κ	-0.684	-0.826	-0.001	-0.655	-0.825	-0.794
f_3 = 0.500	WMR	0.995	0.990	0.614	0.987	0.990	0.936
f_1 = 0.250	OA	-0.545	-0.799	-0.000	-0.528	-0.799	-0.863
f_2 = 0.250	κ	-0.546	-0.801	-0.000	-0.529	-0.801	-0.863
f_3 = 0.500	WMR	0.978	0.987	0.662	0.972	0.987	0.906
f_1 = 0.333	OA	-0.493	-0.758	0.003	-0.408	-0.758	-0.758
f_2 = 0.333	κ	-0.494	-0.759	0.001	-0.409	-0.759	-0.759
f_3 = 0.333	WMR	0.982	0.985	0.710	0.957	0.985	0.953

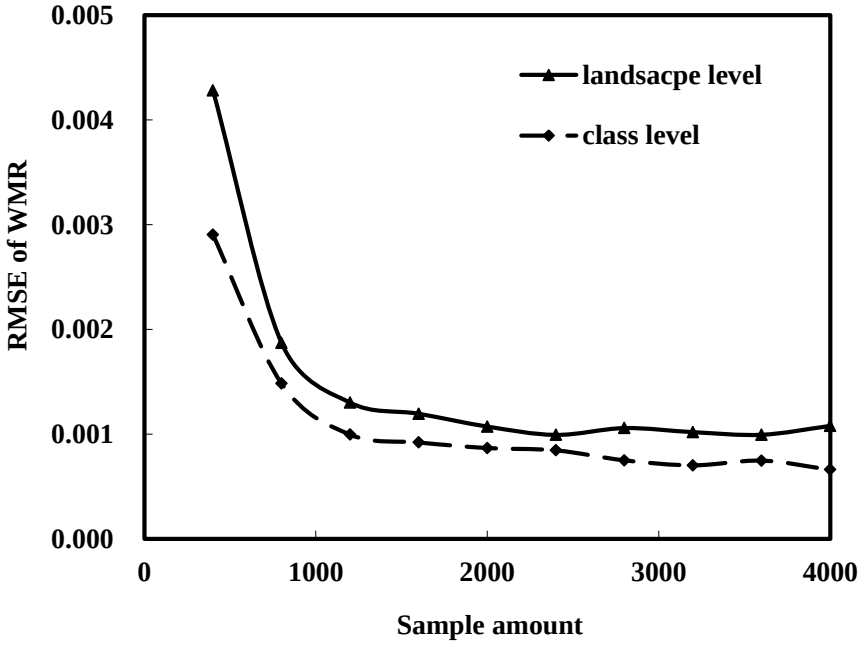

Fig. 2.4 Relationship between RMSE of WMR and the sample amount

2.5 Discussion and Conclusion

Since traditional classification accuracy assessment indices are not well correlated with LPI error, Weighted Misclassification Rate is proposed to clarify the LPI error in this study. WMR is calculated based on the reference data in 3×3 blocks, which can be obtained from high-resolution images, as the same as the validation data for soft classification assessment (e.g. Wu et al., 2003). Through an analysis of a series of simulated images, WMR was found to be well correlated with errors of NP, ED, CONTAG, AI, and DLFD, but not MPS, suggesting that the proposed WMR, as a supplement to the overall accuracy and the kappa coefficient, has the potential to be a useful measure of classification error for landscape analysis. However, since there is still a large gap between such simulated data and the actual data, WMR should be validated using actual data or more elaborate simulations in the future.

CHAPTER 3

An Automated Approach for Updating Land Cover Maps based on Integrated Change Detection and Classification Methods

3.1 Introduction

Information regarding land cover composition and changes is valuable for studying multiple aspects of an environmental system, such as energy balance, biogeochemical cycles, hydrological cycles and the climate system, which are regarded as crucial elements in global change studies (Turner et al. 1995). Therefore, reliable land cover information from remotely sensed data is increasingly required at a continuum of scales, from local and regional to continental and global scales. At global scales, several land cover datasets derived from remotely sensed data are available currently, including IGBP DISCover (Loveland et al., 2000), the MODIS land cover product (Friedl et al., 2002), the UMD land cover product (Hansen et al., 2000), and Global Land Cover 2000 (Bartholomé and Belward, 2005). All of the above datasets are at a spatial resolution of 1 km. Additionally, another global land cover dataset, GlobCover produced by European Space Agency (ESA), is at a resolution of 300 m (Arino et al., 2008). However, previous studies have shown that there is relatively little agreement between these global land cover datasets (Hansen and Reed, 2000; Iwao et al., 2006; Kaptué Tchuenté et al., 2011), which could

decrease the reliability of the related studies. Additionally, these coarse resolution land cover products cannot satisfy the requirements of some specific studies, such as landscape analysis and land resources management at regional scales. Another important issue that has been found in the existing land cover products is that these products are derived only from remotely sensed data acquired during one or several years and represent land cover characteristics for a specific period with a lack of long-term land cover change information. At a regional scale, most land cover/use maps were derived from medium spatial resolution data, such as Landsat, Advanced Space-borne Thermal Emission and Reflection Radiometer (ASTER), and SPOT High-Resolution Visible and Infrared (HRVIR). Although the potential exists to achieve better classification accuracy, much human intervention is required in the classification procedure that cannot satisfy the requirement for the timely extraction of land cover information based on the large and growing satellite data archives of the Earth's surface.

Although many computer-aided techniques have been developed for land cover classification or change detection during the past decades (Canty, 2006; Lu and Weng, 2007; Lu et al., 2004), the skills and experience of an analyst are still very important for the success of image classification (Weng, 2011; Aitkenhead and Aalders, 2011) because the required human intervention is labor consuming and subjective. Moreover, the lack of historical and coincidental ground information to either establish training data or assess identification accuracy also decreases the accuracy of land cover maps

and the flexibility of classification and change detection algorithms (Xie et al., 2010). Therefore, the reliable classification of large amounts of remotely sensed data remains a very challenging task (Franklin and Wulder, 2002).

A promising solution to the aforementioned technical difficulties in land cover map updating is to best utilize a known classification map instead of independently classifying the remotely sensed images. Xian et al. (2009) proposed a technique to update the 2001 national land cover database using a change detection method. In that study, Change Vector Analysis (CVA) was first employed to detect changed areas and then the detected changed areas were reclassified using Decision Tree Classification (DTC). This technique is capable of producing a reasonably accurate land cover map in a cost-effective way. However, CVA has a strict requirement for remotely sensed data that two used images acquired in different years should come from the same phenological period (Chen et al., 2003), which limits its wide application. In many cases, multi-seasonal data are strongly recommended because these data are not only useful for classifying different vegetation types (Saadat et al., 2011; Maxwell et al., 2004) but also for correctly identifying land cover that changes seasonally, such as water bodies and snow cover (Ho and Umitsu, 2011; Negi et al., 2009). Unfortunately, acquiring such data in similar multi-seasons for both of the two years is very difficult because of cloud contamination. Furthermore, a single CVA threshold is not appropriate for detecting the area of different change types (Xian et al., 2009), which increases the difficulty of determining a suitable threshold. Another approach, the

Tempo-Spatial Feature Evolution (T-SFE) model (Xie, 2010), was proposed to address the difficulty of acquiring a historical training dataset for the classification of remotely sensed data. This model first produces the spectral class map by the unsupervised ISODATA classifier and then assigns the spectral class to the ground cover type by referring to a reference map of ground cover types from a subsequent time. Although this method avoids the requirement for a classification training dataset, the T-SFE model is only an exploratory rather than an automatic method because a satisfactory classification result requires the proper calibration of various model parameters.

Although CVA-DTC has limitations, the strategy of updating land cover data only for the changed areas is promising. Therefore, we developed a new approach to update land cover maps by improving the updating strategy of Xian et al. (2009). The proposed approach aims to achieve two objectives: 1) to reduce the CVA requirement for remotely sensed imageries that should be acquired in the same phenological period from different years; and 2) to generate a fully unsupervised, automated method without human interaction for training data collection and parameter calibration. In the proposed approach, the Maximum Likelihood Classifier (MLC), which is the most popular supervised classification method in application studies, is employed for classification. The straightforward change detection technique, Change Vector Analysis in Posterior Probability Space (CVAPS) (Chen et al., 2011) or Post Classification Comparison (PCC), are employed for change detection. Compared with

CVA, PCC and CVAPS have relatively low requirements for remotely sensed data. Data acquired in different seasons or even with different remote sensors can be used (Serra et al., 2003). Considering the cumulative error in PCC (Machleod and Congalton, 1998; Castellana et al., 2007; Chen et al., 2011), CVAPS is recommended here because it can inherit the advantages of CVA and PCC. The greatest challenge in our method is to properly select the training sample. We proposed an iterated procedure to select training samples automatically based on a known classification map to ensure that the method is completely unsupervised. Additionally, an approach based on the Markov Random Fields (MRF) model was employed to reduce the "salt-and-pepper" error that usually occurs in pixel-based classification methods. A case study using Landsat data was conducted to validate the effectiveness of the proposed method, and the new method is expected to be more practicable for land cover updating or historical land cover mapping than CVA-DTC in common application cases with an available land cover map for a certain year.

3.2 Methodology

The proposed approach consists of three main parts: the change detection method, the Markov Random Fields (MRF) model, and an iterated training sample selecting procedure. The general flowchart is shown in Fig. 3.1.

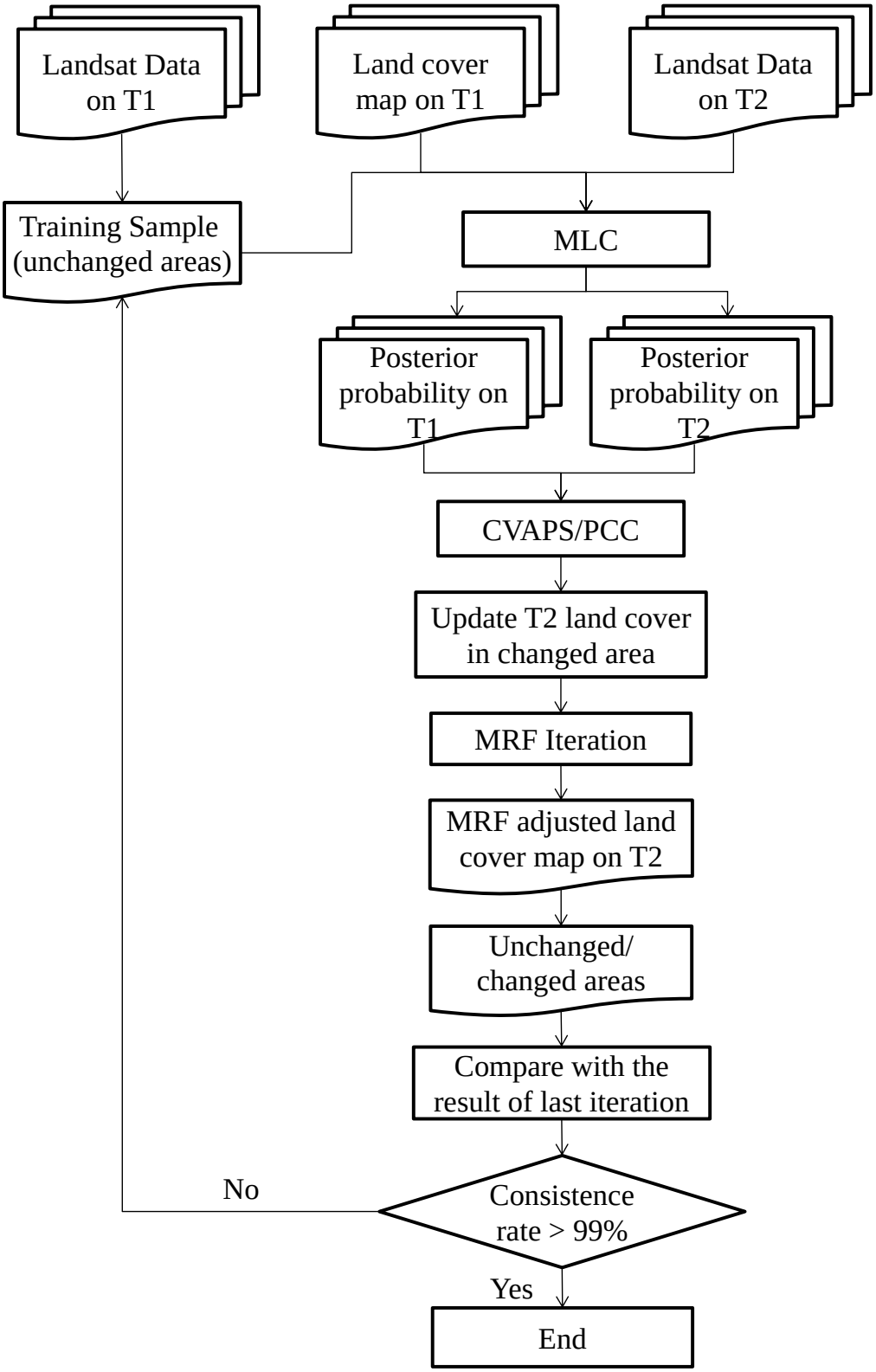

Fig. 3.1 Flowchart of the proposed approach

3.2.1 Change Detection Method

The change detection methods can be categorized into two types: 1) methods based on the radiometric difference between different acquisition dates, such as CVA; and 2) methods based on the classification results of the satellite images, such as PCC and CVAPS. The former method requires the used data should be acquired in the same phenolgoical period and from the same remote sensors. In contrast, the latter methods which do not have such strict requirement were selected in this study. PCC detects the changed areas by directly comparing two classification maps. This method is straightforward and easily conducted but suffers from cumulative error (Chen et al., 2003; Liu et al., 2006; Castellana et al., 2007; Chen et al., 2011).

As an improvement, CVAPS compares the posterior probability maps for two different dates instead of the classified maps, which avoids cumulative error (Chen et al., 2011). Supervised classifiers can be used to estimate the posterior probabilities of different land cover types. Here，a standard Maximum Likelihood Classifier (MLC) was used for its high computing efficiency and acceptable accuracy. In MLC, the normal distribution model is adopted. Assuming that the posterior probability vectors of a pixel at times 1 and 2 are $\mathbf{P}^{(1)}$ and $\mathbf{P}^{(2)}$, respectively, the change vector in a posterior probability space can be defined as

$$\begin{aligned}\Delta\mathbf{P} &= \mathbf{P}^{(2)} - \mathbf{P}^{(1)} \\ &= \begin{pmatrix} p_1^{(2)} \\ p_2^{(2)} \\ \cdots \\ p_m^{(2)} \end{pmatrix} - \begin{pmatrix} p_1^{(1)} \\ p_2^{(1)} \\ \cdots \\ p_m^{(1)} \end{pmatrix}\end{aligned} \tag{3-1}$$

where *m* is the number of classes. **ΔP** represents the difference in the posterior probability of each class for the two dates and contains the change information between the two images. The change magnitude of the vector is calculated as

$$\|\Delta\mathbf{P}\| = \sqrt{\sum_{i=1}^{m}\left(p^{(2)}{}_i - p^{(1)}{}_i\right)^2} \tag{3-2}$$

Compared with CVA, ||**ΔP**|| of different change types are at the same scale because the posterior probability can normalize the intra-class variability and inter-class distance. When the ||**ΔP**|| value is greater, the probability of change is higher. Compared with PCC, CVAPS requires a threshold to determine the changed/unchanged pixels. The threshold can be determined by either a supervised or unsupervised method. Here, the unsupervised threshold determination method based on the histogram entropy (Kapur et al., 1985) was employed to ensure that the method was unsupervised, although the supervised method is capable of achieving higher change detection accuracy (Chen et al., 2011).

Although some non-parametric classification algorithms, such as Support Vector Machine (SVM) and Artificial Neural Net (ANN), have been found to perform better than MLC in some studies (e.g., Dixon and Candade, 2007,; Mountrakis et al., 2011), these algorithms were not considered in this study because their computation cost increases geometrically with the increase in training sample size.

3.2.2 Markov Random Fields Model

Pixel-based change detection (or classification) methods usually generate more "salt-and-pepper" error (Lu and Weng, 2007). One solution is to employ an object-based classification method, which has recently received increasing attention (Blaschke, 2010). However, such methods require many parameters, which are usually difficult to determine and do not satisfy the requirements of our automated method. Another solution is post-classification processing, such as the majority filter and the MRF model. In the past decades, the MRF model has been introduced in many change detection studies and has been shown to be effective at reducing "salt-and-pepper" error (e.g., Jeon and Landgrebe, 1991; Solberg et al., 1996; Bruzzone and Prieto, 2000; Liu et al., 2008). Compared to the object based classification method, the MRF model requires fewer parameters and has greater computing efficiency because parallel computing and advanced optimization algorithms are available for the MRF model (Sui et al., 2011; Szeliski et al., 2008). Therefore, the MRF model introduced in Bruzzone and Prieto (2000) was employed to reduce the "salt-and-pepper" error. In the MRF model, the probability (P) of the pixel (i, j) belonging to the class C is determined by both the spectral information and the labels of the neighboring pixels:

$$P\left(C(i,j)\right)=\frac{1}{Z}\exp\left\{-\left(U_{\text{context}}[C(i,j)]+U_{\text{spectrum}}[C(i,j)]\right)\right\} \tag{3-3}$$

where Z is the normalizing constant; U_{context} and U_{spectral} is the energy of the context and the spectrum, respectively. The energy of the spectrum is the logarithmic function of the posterior probability:

$$U_{\text{spectrum}}[C(i, j)] = -\ln\left(p_{\text{spectrum}}[C(i, j)]\right) \tag{3-4}$$

where p_{spectral} is the posterior probability that is derived from the MLC classifier. The energy of the context is calculated based on the labels of the neighboring pixels. For the target pixel (i, j), a set of neighbor pixels called $\mathbf{N}(i, j)$, is defined first. As is the case in previous studies, a second-order neighborhood set (Fig. 3.2) is employed:

$$\mathbf{N}(i, j) = \{(i \pm 1, j), (i, j \pm 1), (i + 1, j \pm 1), (i - 1, j \pm 1)\}. \tag{3-5}$$

(i-1, j-1)	(i, j-1)	(i+1, j-1)
(i-1, j)	(i, j)	(i+1, j-1)
(i-1, j+1)	(i, j+1)	(i+1, j+1)

Fig. 3.2 Second-order neighborhood set used by the MRF model

Then the energy of the context is calculated as follows:

$$U_{\text{context}}[C(i, j)] = U_{\text{context}}\left(C(i, j) \mid \{C(g, h), (g, h) \in \mathbf{N}(i, j)\}\right) = \sum \beta \delta_k \left(C(i, j), C(g, h)\right) \tag{3-6}$$

where

$$\delta_k \left(C(i, j), C(g, h)\right) = \begin{cases} -1, & \text{if } C(i, j) = C(g, h) \\ 0, & \text{if } C(i, j) \neq C(g, h) \end{cases}, \tag{3-7}$$

and β is the weight coefficient of the context information. Here, this value was set as 1.6 based on the study of Bruzzone and Prieto (2000). The MRF model determines the class by minimizing the energy function (equivalent to maximizing the probability function) in Eq. (3-3) using the optimization algorithm such as iterated conditional modes (ICM), metropolis, graph cuts, and loopy belief propagation (LBP) (Besag, 1986; Kohli et al., 2007; Szeliski et al., 2008). In this paper, the traditional ICM algorithm was employed for its acceptable efficiency and accuracy in the classification of remotely sensed images (Bruzzone and Prieto, 2000; Liu et al., 2008). It is noticed that only the changed pixels detected in Section 3.2.1 were refined by MRF model. The iteration of ICM can be described as follows:

1) For all changed pixels determined by the pixel-based change detection technique, initialize $C(i, j)$ with the class that minimizes the spectral energy function. The initialized classification is equal to the MLC result.
2) For all changed pixels, update $C(i, j)$ to the class that minimizes the total energy function (Eq. 3-3).
3) Repeat Step 2 until convergence is reached.

After iteration, the isolated changed pixels are more likely to be marked as unchanged pixels; therefore, the "salt-and-pepper" error can be reduced.

3.2.3 Training Sample Selection

The key step of the automated approach is the proper selection of the training samples because they are required for MLC, PCC and CVAPS. Traditionally, the training samples are selected manually depending on the knowledge of the analyst or field investigation, which is time-consuming and subjective. It is assumed that the remotely sensed images were acquired in the year of T1 and T2 respectively and a classification map is already available on T1. The training sample for T2 is selected based on the known classification map on T1. Usually, the land cover changes only occurred in small areas between T1 and T2 for most applications, consequently, the use of the unchanged areas as training samples for the image on T2 is reasonable. Therefore, we developed an iterated method to refine the unchanged area as training samples. For convenience of description, the image data on T1 and T2 are denoted as $\mathbf{\Psi}_1$ and $\mathbf{\Psi}_2$, and the classification maps on T1 and T2 are denoted as $\mathbf{C}_1$ and $\mathbf{C}_2$. The training sample set is denoted as $\mathbf{\Omega}$. The iteration procedure includes following steps:

1) All of the pixels in the known classification map on T1 are first selected into training samples set: $\mathbf{\Omega} = \mathbf{C}_1$.
2) The $\mathbf{\Omega}$ is used for training the MLC for the calculation of posterior probability vectors on T1 and T2
3) Changed /unchanged areas are detected by a pixel-based change detection method (CVAPS or PCC). The sets of changed pixels and unchanged pixel are denoted as $\mathbf{\Theta}_c$ and $\mathbf{\Theta}_u$

4) The T2 land cover types of the changed pixels $\mathbf{C}_2(\mathbf{\Theta}_c)$ are updated according to the MLC results, and unchanged pixels $\mathbf{C}_2(\mathbf{\Theta}_u)$ inherit the land cover labels from the T1 land cover map.

$$\begin{cases} \mathbf{C}_2(\mathbf{\Theta}_c) = \mathrm{MLC}(\mathbf{\Omega}, \mathbf{\Psi}_2, \mathbf{\Theta}_c) \\ \mathbf{C}_2(\mathbf{\Theta}_u) = \mathbf{C}_1(\mathbf{\Theta}_u) \end{cases} \tag{3-8}$$

5) The T2 land cover map $\mathbf{C}_2 = \{\mathbf{C}_2(\mathbf{\Theta}_c), \mathbf{C}_2(\mathbf{\Theta}_u)\}$ is refined using the MRF model

$$\mathbf{C}_{2M} = \mathrm{MRF}(\mathbf{C}_2)\,, \tag{3-9}$$

and a more aggregate changed/unchanged map is obtained by comparing $\mathbf{C}_{2M}$ and $\mathbf{C}_1$. The sets of unchanged pixels and changed pixels are refined as $\mathbf{\Theta}_{uM}$ and $\mathbf{\Theta}_{cM}$

6) The unchanged pixels are re-selected as training samples $\mathbf{\Omega} = \mathbf{C}_1(\mathbf{\Theta}_{uM})$ and goto step (2)

The Step (2) to (6) is repeated until the $\mathbf{\Theta}_{uM}$ and $\mathbf{\Theta}_{cM}$ are highly consistent with the result of last iteration at the rate of 99%. The consistence rate is defined as:

$$\text{Consistence Rate} = \frac{p_{\text{unchanged}} + p_{\text{changed}}}{P}\,, \tag{3-10}$$

where $p_{\text{unchanged}}$ is the number of pixels that are marked as unchanged pixels in both iterations, and p_{changed} is the number of pixels that are marked as changed pixels in both iterations. P is the number of all of the pixels in the image. Consequently, a higher consistency rate indicates that a change in the training samples has less influence on the changed/unchanged pixel detection result. This iterated procedure is expected to refine the unchanged area as the training samples improve classification

accuracy. After iteration, the final changed/unchanged map and the T2 classification map are obtained.

3.3 Case Study

3.3.1 Data and Study Area

A case study on the Landsat data was conducted to validate the effectiveness of the proposed approach. The study area is located in Xi'an city, Shaanxi province, China (34°16'N, 108°54'E). Similarly to other cities in China, the urban area of Xi'an city expanded rapidly in the last decade along with the rapid economic growth in the area. The Landsat ETM+ images acquired on 2000-06-29 and 2000-11-20 and the Landsat TM images acquired on 2010-06-17 and 2010-08-04 were used for this experiment (Fig. 3.3). The size of the images was 1200×1300 pixels, covering an area of approximately 1400 km^2. Multi-seasonal TM data were collected because these data are useful for distinguishing the cropland and forest. The forest pixels have a longer greenness period from May to October, whereas the cropland pixels have low greenness in June but approach the maximum of the growth in August. In the winter, both of the cropland and forest wilt and exhibit similar spectral characteristics. Therefore, cropland and forest pixels are particularly difficult to distinguish in the winter. CVA cannot be used in this case study because the multi-seasons in 2000 and 2010 did not correspond with each other.

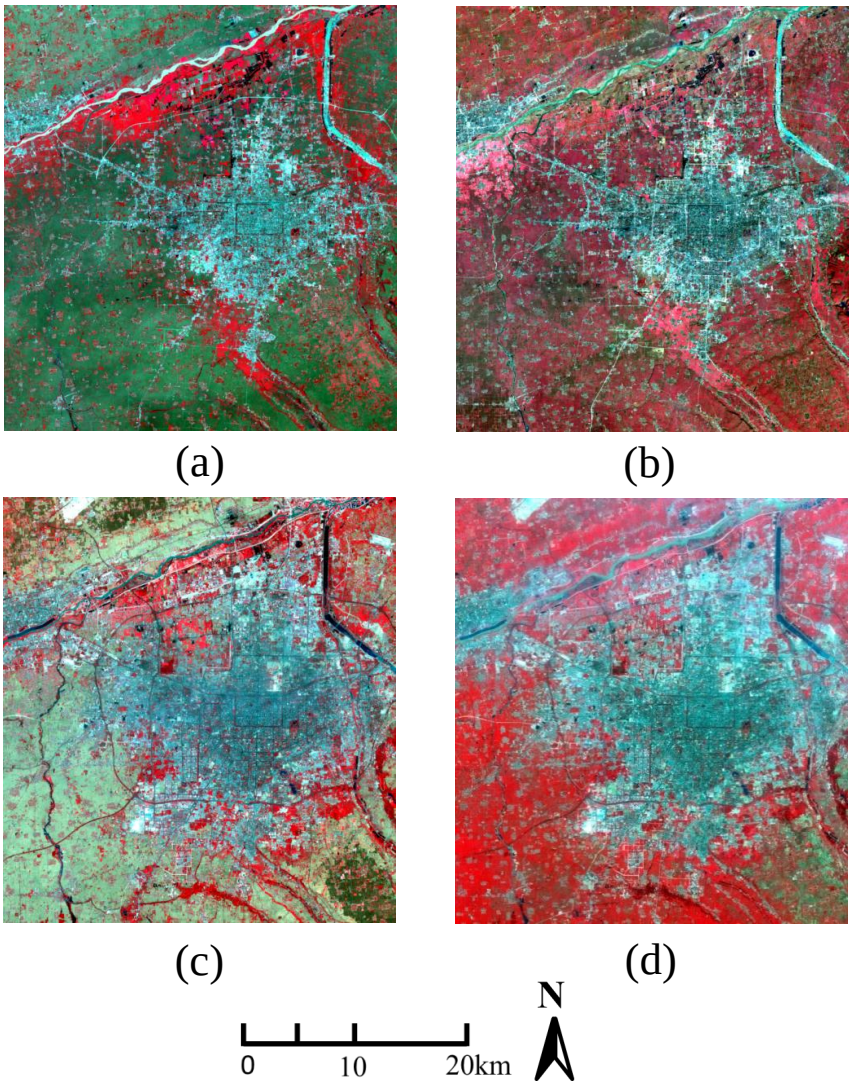

Fig. 3.3 Landsat TM/ETM+ images of the study area (a. ETM+ on 2000-06-29; b. ETM+ on 2000-11-20; c. TM on 2010-06-17; d. TM on 2010-08-04)

A known classification map for one year is required for the proposed methodology. Here, we acquired the land cover map for 2010 (Fig. 3.4) from the National Geoinformatics Center of China, which was generated from TM data by visual interpretation referring to the high spatial resolution images (QuickBird).

According to the land cover map, there were five land cover types in the study areas including bareland, cropland, forest, urban and water.

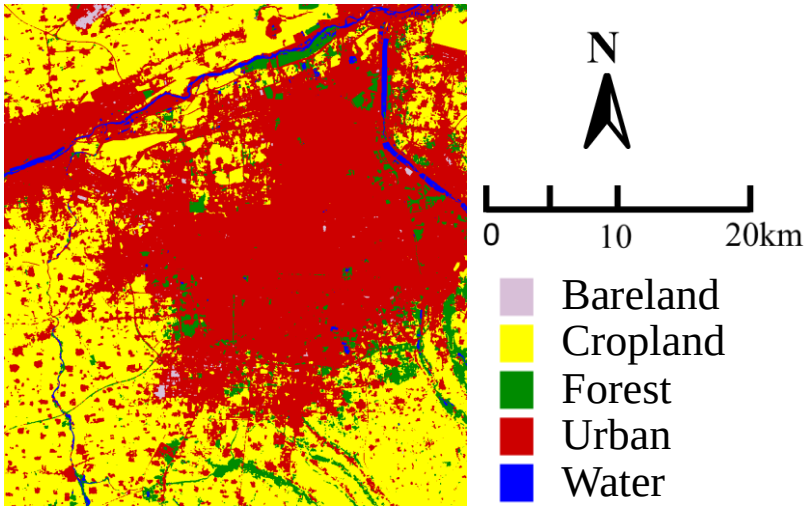

Fig. 3.4 Land cover map in 2010

3.3.2 Updating Results and Accuracy Assessment

The land cover map in 2000 was updated based on the multi-seasonal Landsat data and the land cover map in 2010 using the proposed method. We did not update chronologically from 2000 to 2010; instead, updated in the reverse order because the known land cover map was available in 2010. The change detection methods PCC and CVAPS were both tested for comparison. As shown in Fig. 3.5, the results derived from these methods based on PCC and CVAPS were very similar and exhibited a very high agreement of 97%. From 2000 to 2010, the most obvious change was urban expansion by encroaching areas with other land cover types correspondingly.

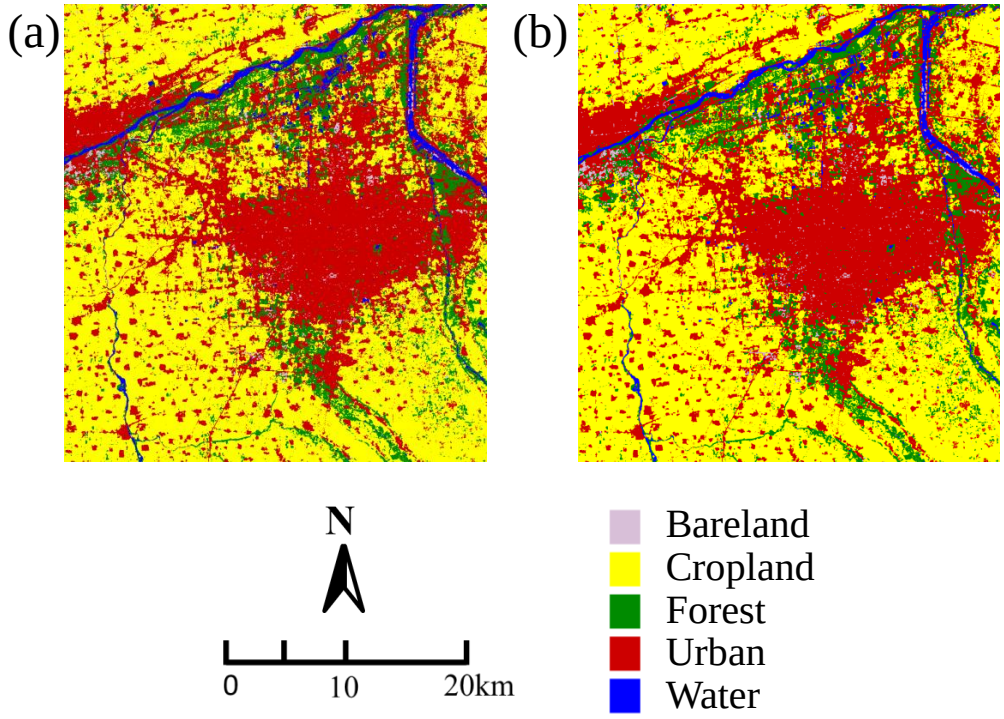

Fig. 3.5 Land cover map in 2000 updated by the approach based on CVAPS (a) and by the approach based on PCC (b)

For quantitative accuracy assessment, 6398 pixels in the 2000 image were randomly selected for validation. These pixels were interpreted visually based on the experience of the author's group and reference data from 2000. The accuracies of "change/unchanged" were examined first because change detection is an important part of this methodology. As shown in Tables 3.1 and 3.2, the methods based on CVAPS and PCC produced similar results, whereas PCC estimated slightly more changed areas than the CVAPS results, which is consistent with the results of a previous study (Chen et al., 2011). For classification accuracy, the confusion matrixes are shown in Tables 3.3 and 3.4. The accuracies of the two methods are also similar,

while the method based on CVAPS performs slightly better. The structures of the two confused matrices are also similar. In detail, the water has the highest classification accuracy because the water spectrum is stable and unique, whereas there were much misclassification between forest and cropland, and between urban and bareland because of similar spectra. Additionally, there was also misclassification between urban and forest because trees usually cover the small towns, which results in a strong spectral vegetation signal in some urban pixels.

Table 3.1 “Changed/unchanged” confusion matrix of the approach based on CVAPS

Number of pixels		Reference changed			
		Unchanged pixels	Changed pixels	Sum	Commission error
Classified changed	Unchanged pixels	4002	600	4602	13.0%
	Changed pixels	230	1557	1787	12.9%
	Sum	4232	2157	6389	
	Omission error	5.43%	27.8%		
Overall accuracy 87.01%，kappa coefficient 0.697					

Table 3.2 “Changed/unchanged” confusion matrix of the approach based on PCC

Number of pixels		Reference changed			
		Unchanged pixels	Changed pixels	Sum	Commission error
Classified changed	Unchanged pixels	3927	567	4494	12.6%
	Changed pixels	305	1590	1895	16.1%
	Sum	4232	2157	6389	
	Omission error	7.2%	26.3%		
Overall accuracy 86.3%，kappa coefficient 0.686					

Table 3.3 Classification confusion matrix of the approach based on CVAPS

Number of pixels		Reference						
		Bareland	Cropland	Forest	Urban	Water	Sum	Commission error
Classification	Bareland	325	10	40	24	1	400	18.8%
	Cropland	7	1899	190	105	1	2202	13.8%
	Forest	0	187	958	0	13	1158	17.3%
	Urban	92	69	124	1834	39	2158	15.0%
	Water	9	1	13	1	456	480	5.0%
	Sum	433	2166	1325	1964	510	6398	
Omission error		24.9%	12.3%	27.7%	6.6%	10.6%		
Overall accuracy 85.5%，kappa coefficient 0.802								

Table 3.4 Classification confusion matrix of the approach based on PCC

Number of pixels		Reference						
		Bareland	Cropland	Forest	Urban	Water	Sum	Commission error
Classification	Bareland	328	10	43	21	1	403	18.6%
	Cropland	7	1841	177	104	1	2130	13.6%
	Forest	0	204	967	0	15	1186	18.5%
	Urban	89	110	124	1838	42	2203	16.6%
	Water	9	1	14	1	451	476	5.3%
	Sum	433	2166	1325	1964	510	6398	
Omission error		24.2%	15.0%	27.0%	6.4%	11.6%		
Overall accuracy 84.8%，kappa coefficient 0.793								

3.3.3 Role of Iterated Training Sample Selecting Procedure

As a key component of the proposed methodology, the effect of the iterated training sample selecting procedure was investigated. Fig. 3.6(a) shows the relationship between the iteration number and consistence rate. The iteration ended when the consistence rate reached 99%. Both approaches that were based on CVAPS and PCC converged rapidly at the fifth and fourth iterations, respectively. This result

indicates that the proposed approach does not significantly increase the computational cost.

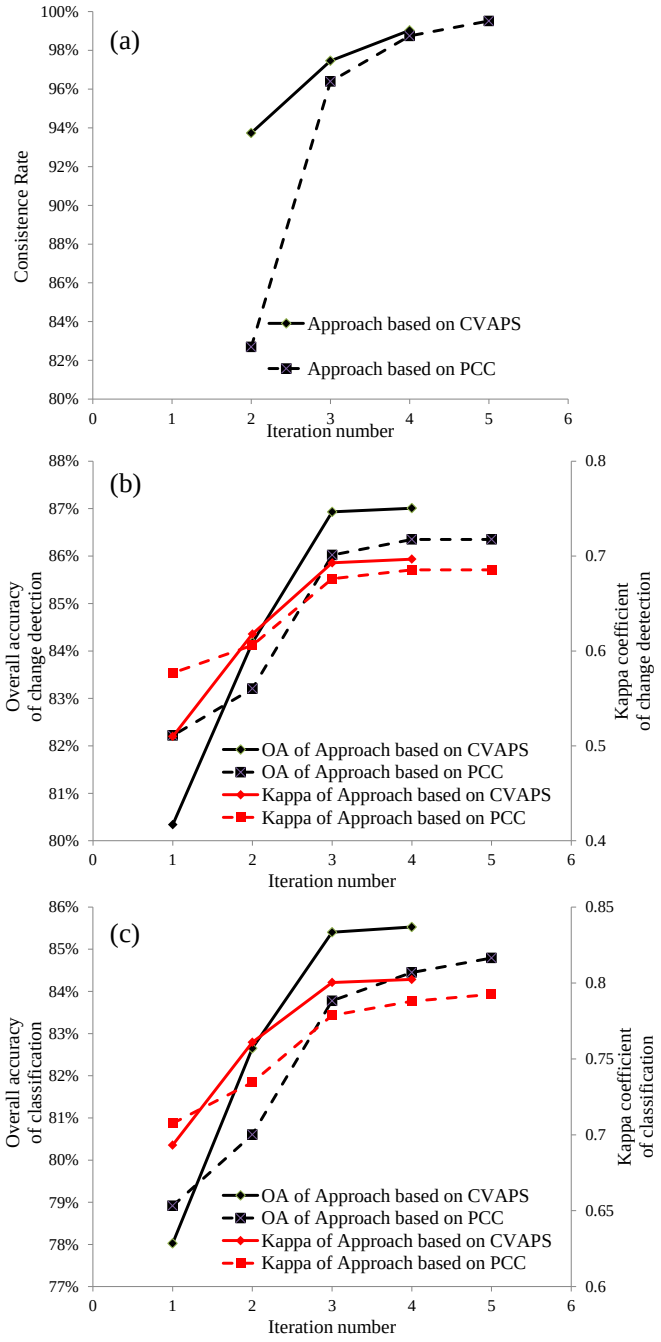

Fig. 3.6 Relationship between iteration number and consistence rate (a), accuracy of change detection (b), and accuracy of classification (c)

As shown in Fig. 3.6 (b) and (c), the iteration largely improved the change detection and classification accuracies by more than 5% for Overall Accuracy (OA) and 0.1 for Kappa coefficient. These results indicate that the proposed iterated training sample selecting process can refine the training sample and improve the change detection and classification accuracy.

3.3.4 Role of MRF model

The methods with and without the MRF model were compared. Fig. 3.7 shows the updated land cover maps produced by the CVAPS-based approaches with and without the MRF model. As shown in Fig. 3.7, the approach with the MRF model produced more aggregated results, and the "salt-and-pepper" error was reduced largely. The results of the PCC-based approaches are comparable, and the data are not shown in the figures. Fig. 3.8 compares the quantitative classification accuracies of the approaches with and without the MRF model. The MRF model improved the overall classification accuracy by approximately 5% and the kappa coefficient by approximately 0.07. The approaches based on CVAPS and PCC produced almost the same results. A limitation of the MRF model is that some thin linear objects may be removed. As shown in Fig. 3.9, one traffic road disappeared as the result of using the method with the MRF model. However, we still suggest using the MRF model because the classification accuracy can be improved significantly.

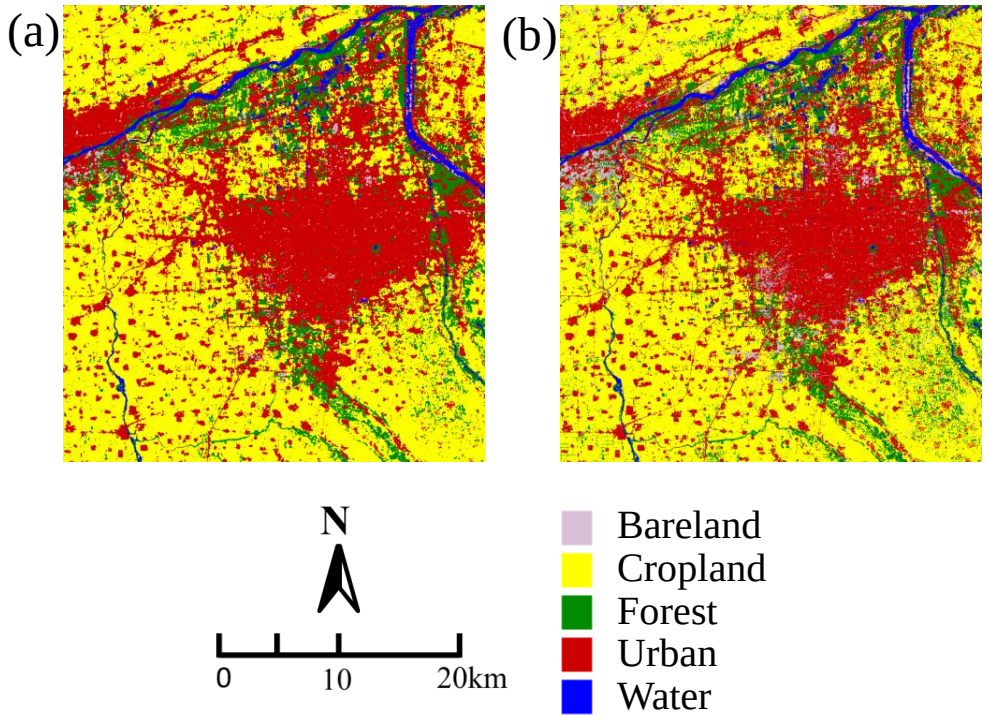

Fig. 3.7 Land cover map in 2000 updated by the approach of CVAPS with MRF model (a) and without MRF model (b)

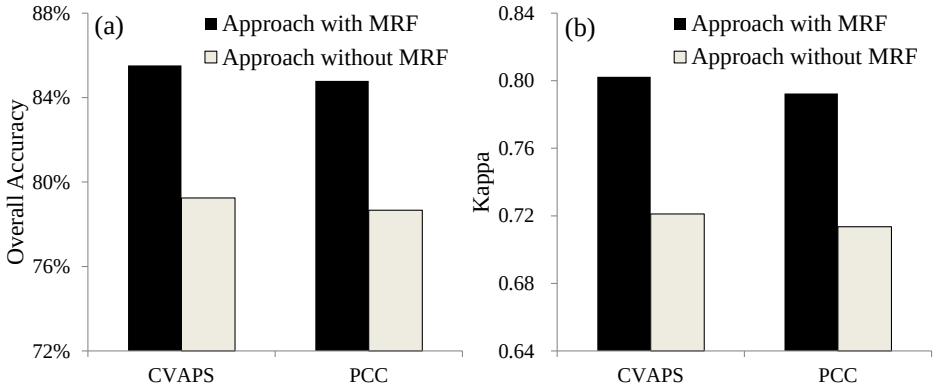

Fig. 3.8 Comparison of the classification accuracies of the proposed approaches with and without the MRF model (a. overall accuracy; b. kappa coefficient)

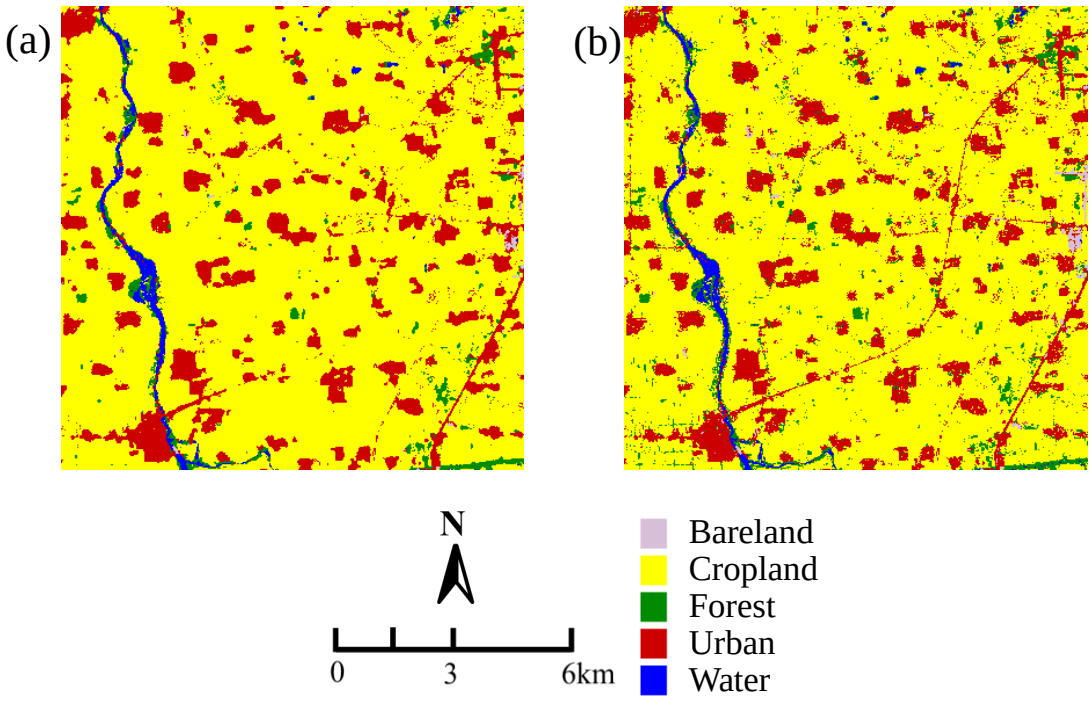

Fig. 3.9 Detailed comparison of the approaches with and without the MRF model (a. with MRF model; b. without MRF model)

3.3.5 Role of multi-seasonal data

Compared to CVA-DTC, the proposed approach is more suitable to multi-seasonal data. Therefore, we investigated whether multi-seasonal data can improve the classification accuracy compared with single-seasonal data. Here, four single-seasonal data combinations were tested, including the images acquired on 2000-06-29 and 2010-06-17; 2000-06-29 and 2010-08-04; 2000-11-20 and 2010-06-17; and 2000-11-20 and 2010-08-04. The accuracies are compared in Fig. 3.10. The results derived from the multi-seasonal data achieved the highest accuracy. This is reasonable because multi-seasonal data contains phenological information,

which is very useful for distinguishing the cropland and forest. In cases of single-seasonal data, the accuracy decreased to varying extents. In particular, the accuracy decreased largely (approximately 10% of overall accuracy and 0.10 of kappa) when TM data acquired in the winter (2000-11-20) was used. This is because cropland is very easily misclassified with deciduous forest in the winter. In most cases, the method based on CVAPS performed better than the method based on PCC. Therefore, we suggest using CVAPS in application studies.

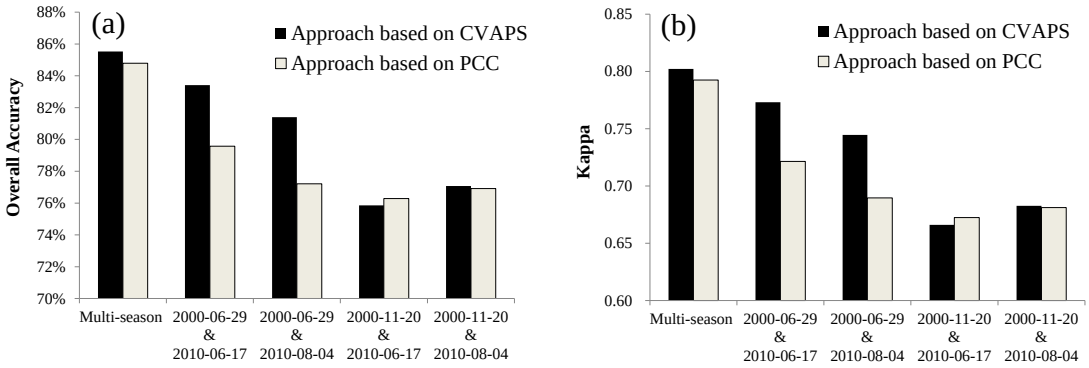

Fig. 3.10 Accuracies of classification results based on multi-seasonal and single-seasonal data (a. overall accuracy; b. kappa coefficient)

3.4 Discussion and Conclusion

The proposed approach uses a similar CVA-DTC strategy as Xian et al. (2009), which updated the classification map only for the changed areas. In this study, CVA was replaced with more applicable change detection techniques, CVAPS or PCC, and replaced DTC with MLC to widen the scope of its flexibility. An iterative training

sample selection procedure was proposed by appropriately utilizing the unchanged area between two years to address the challenge of selecting the proper training samples without supervision. The experimental result shows that this iterative procedure can improve classification accuracy by approximately 5%. Furthermore, the iterative process converges in no more than five iterations, suggesting a low computational cost.

In comparison to CVA-DTC, the proposed approach employed CVAPS or PCC to detect changed areas instead of directly comparing the radiometric difference between different acquisition dates. Therefore, this method can avoid the strict requirement of CVA for reliable image radiometric correction and remotely sensed data acquisition that the two images acquired in different years should be from the same phenological period. Without such strict requirements, the proposed approach can be applied for land cover mapping or updating over larger scales and for longer periods. Additionally, the change magnitudes of different change types in CVAPS are on the same scale because the posterior probability for each pixel classification is in the range of zero to one. Consequently, a single threshold is more suitable for CVAPS than CVA, which is convenient for users to optimize the threshold with the existing thresholding methods. Compared with PCC, CVAPS analyzes the posterior probability vector with CVA, which can alleviate classification error accumulation effectively existing in PCC and improve the changed/unchanged detection accuracy.

As shown in Section 3.3.5, CVAPS performs better than PCC in most cases. Therefore, CVAPS is recommended in applications.

In this study, MLC was employed as the supervised classification method. This method is popular and easily conducted but requires training data. In this study, an iterative training sample selecting procedure was proposed to address the limitation by appropriately utilizing the unchanged area between two years. The first step in the procedure is to use the entire known land cover map as the training data, which provides huge training samples. In the subsequent steps, the change detection result is used to refine the training samples and ensure that only unchanged pixels are used as the training reference. Regardless of the number of times the iteration is performed, the size of training samples for classification is still very large, which is nearly equal to the size of the unchanged area. MLC is more suitable for such large training samples because the huge size of training samples is more likely to satisfy the normal distribution assumed in MLC. The advantage of the non-parameter classification algorithms, such as SVM and ANN, is the low requirement for specific spectral distribution. Another advantage of SVM is its robustness for the small training sample size. These advantages are not shown obviously in the case of a large sample size. Instead, the computation cost increases geometrically with the increase in training sample size. Therefore, the non-parameter algorithms are not considered in this approach. However, any supervised classifiers can be used in our approach in theory. In the future, more advanced classifiers can be employed.

MRF model is also an important sub-module in this approach. The experiment result shows that it can reduce "salt and pepper" error significantly although some thin linear objects may also be removed mistakenly. In this study, a standard MRF model was employed for general feasibility. However, if some prior knowledge, for example the land cover incompatible/compatible rules among spatial or temporal neighborhood pixels, are available (Liu et al., 2006, Liu et al., 2008), they also can be integrated into the MRF model to meet the specific need of a study.

In practice, updating a land cover map often depends on data availability and quality, time and cost constraints, and analytical skill and experience. Compared with CVA-DTC and T-SFE, the proposed approach requires no supervision and decreased requirements for remotely sensed data, which is applicable to timely updates of both historical and future land cover maps.

We also recognize that there are potential limitations regarding this new approach. Firstly, this approach assumes the same classification systems between two years. Therefore, the new land cover type will not be correctly identified if it is not available on T1 but appears on T2. In this case, the new land cover type on T2 should be firstly identified before using the proposed approach. One-class classifier (e.g. Muñoz-Marí et al., 2010) may be a good choice for identifying the new land cover type because only the training sample of the new class is required. Another limitation is that the approach does require the availability of one reliable land cover map that provides initial training samples. In general, a high quality classified map is expected. When

the amount of misclassification pixels accounts only for a small proportion, the estimation of mean value and covariance of each class in MLC will be affected very slightly; consequently, the posterior probability calculated from MLC will also be affected slightly. However, if the classification accuracy of the known land cover map is poor, the accuracy of both change detection and classification may be reduced. The impact of error propagation could be complicated, depending on the spectral and spatial distribution of the misclassification pixels. Some possible solutions include selecting core areas of different land cover types in the known map as a training reference instead of using the entire map in the first step or manually selecting the areas with lower classification uncertainty if such information is available.

CHAPTER 4

Soft Image Segmentation Model

4.1 Introduction

With the development of remote sensors with high spatial resolution (around 1 meter) such as IKONOS, QuickBird, Worldview, etc., pixel based image analysis method cannot satisfy the need of high-resolution image processing because the sizes of most land cover objects are much larger than the high spatial resolution. Therefore, object based methods have received more and more attentions recently (Blaschke, 2010). The first and the most important step of the object based method is image segmentation which subdivides an image into a set of non-overlapping "homogeneous" objects (patches). Till now, many image segmentation algorithms have been developed from different perspectives (Haralick and Shapiro, 1985; Dey et al., 2010). The segmentation algorithms can be divided into four categories: (a) point-based, (b) edge-based, (c) region-based and (d) combined (Schiewe, 2002), or categorized as model driven and image driven approaches (Guindon, 1997), depending on different categorization perspectives. Among them, the commercial software, named eCognition (Definiens, 2009) was particularly widely applied in the studies of object based analysis because of its convenience of operation and the effective algorithm of Multi-resolution image segmentation (Blaschke, 2010). The uncertainty is well known come along with the segmentation procedure. The reliabilities of different objects are

different depending on the degrees of homogeneity, and the mixed pixels on the borders between different objects are difficult to be assigned to a certain object. Unfortunately, few studies cared about the uncertainty in image segmentation except of the study of Lucieer and Stein (2002), which proposed a boundary stability image (BSI) to describe the uncertainty of the objects by considering the stability of the boundary. However, it did not consider the potential overlapping between the objects. Based on the idea of soft classification which assigns one pixel into multi classes instead of a single class, this study proposed a soft segmentation model which assigns each pixel into several adjacent objects with corresponding probabilities. The uncertainty of segmentation is reflected in the probability image.

In this paper, the multi-resolution segmentation in eCognition was briefly introduced in section 4.2; and the principle of soft segmentation model was described in detail in section 4.3; a case study of an IKONOS image was conducted for validating the effectiveness of the model in section 4.4; then discussion and conclusion were summarized in section 4.5.

4.2 Multi-resolution Segmentation in eCognition

The multi-resolution segmentation algorithm in eCognition is a bottom-up approach and follows a pair-wise region merging process (Baatz, 2000). At each step, a pair of image objects is merged into one larger object. The merging decision is based on local homogeneity criteria describing the similarity of adjacent image

objects. In eCognition, both of the shape compactness and spectral smoothness are used for determining the degree of homogeneity. The pair is merged when both of two conditions are satisfied: (1) the homogeneity of the merging of the selected pair is maximum among all possible merging pairs; and (2) the homogeneity due to the merging of the selected pair is higher than a threshold of the scale parameter. The second condition determines when the merging procedure stops. Depending on the different scale parameters, segmented image on different levels can be acquired. As shown in Fig. 4.1, spatially, the objects on the low level are subsets within the objects on the high level.

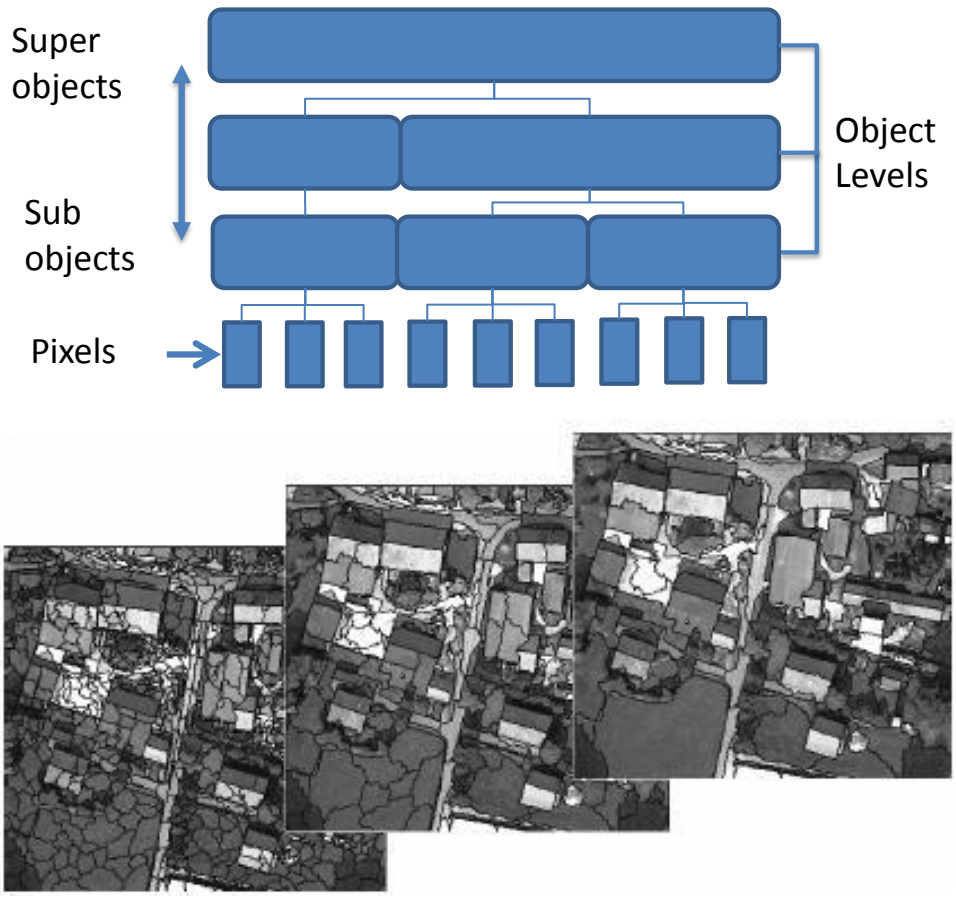

Fig. 4.1 Illustration of multi-resolution segmentation

4.3 Soft Segmentation Model

The soft segmentation model was developed based on the multi-resolution segmented result. Assumed that there are l levels of segmented images (L=1, …, l), L=1 is the pixel level and L=l is the top level. The proposed model aims to produce the probability of each pixel merged into each object on the top level of L=l. The model consists of two steps.

Step 1: The first step of the model is to calculate the probabilities of each sub-object on the level of L=k merged into the super-objects on the level of L=k+1. In eCognition, the ith object on the level of L=k (denoted as i_k) is merged into a single father object on the level of L=k+1. In this model, the i_k is not only probably merged into its father object, but also probably merged into its neighbored objects on level of L=k+1, which are spatially adjacent with i_k (Fig. 4.2). The father object and neighbored objects of i_k on level of L=k+1 are denoted as a set $\mathbf{N}(i_k)$. Therefore, the object i_k has the probabilities of being merged into each object m_{k+1} in the set $\mathbf{N}(i_k)$. The probabilities are calculated based on the principle of Maximum Likelihood, where mean value and covariance are considered. The probability ($p_{i_k,m_{k+1}}$) of object i_k merged into object m_{k+1} is calculated as followed:

$$p_{i_k,m_{k+1}} = p(i_k \mid m_{k+1}) / \sum_{\forall m_{k+1} \in \mathbf{N}(i_k)} p(i_k \mid m_{k+1}) \tag{4-1}$$

where

$$p(i_k \mid m_{k+1}) = \frac{1}{(2\pi)^{p/2} (S_{m,k+1})^{1/2}} e^{-(\boldsymbol{\mu}_{i,k} - \boldsymbol{\mu}_{m,k+1})' S_{m,k+1}^{-1} (\boldsymbol{\mu}_{i,k} - \boldsymbol{\mu}_{m,k+1})/2} \tag{4-2}$$

where $\mu_{i,k}$ and $\mu_{m,k+1}$ are the mean value of object i_k and m_{k+1}; $S_{m,k+1}$ is the covariance matrix of object m_{k+1}.

An example is shown in Fig. 4.2, object 2_k on level of $L=k$ has the probabilities of being merged into the object 1_{k+1} and 2_{k+1} on level of $L=k+1$. When the probability of a sub-object merged into its father object is higher, this step of merging is more reliable.

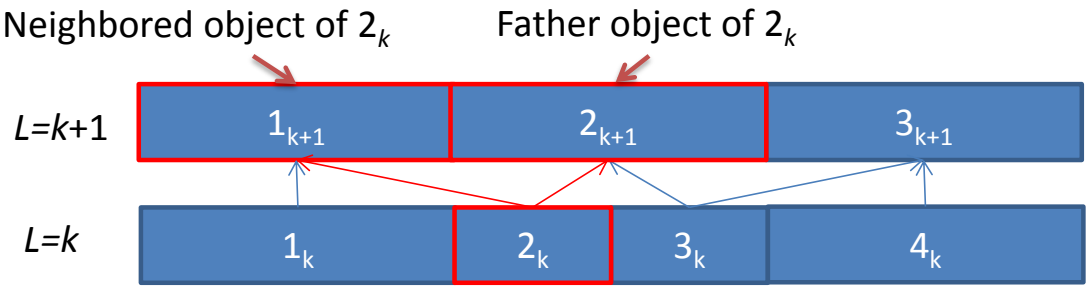

Fig. 4.2 Illustration of the probability of sub-object on level of $L=k$ merged into the super-object on level of $L=k+1$

Step 2: After finishing the first step, we aim to calculate the final probability of each pixel merged into the object on the top level of $L=l$. The probability of the pixel i_1 merged into object m_l on the top level is calculated based on the merging path:

$$P_{i_1->m_l} = \sum_{\forall n->m_l} p_{i,n,1} p_{i,n,2} \cdots p_{i,n,(l-1)} \tag{4-3}$$

where $p_{i,n,1}$,…, $p_{i,n,(l-1)}$ are the probabilities on the nth merging path from pixel i_1 to the object m_l. The product of these probabilities is the probability of the pixel i_1 merged into the object m_l by the nth merging path. Because there may be several

merging paths from pixel i_1 to the object m_l, the final probability of the pixel i_1 merged into the object m_l is the summation of the probabilities on all the merging paths from pixel i_1 to the object m_l.

An illustration is shown in Fig. 4.3. The four pixels on the level of L=1 is merged into two objects on the top level of L=3. The number on the array means the probability of each sub-object merged into the super-object on the next level. And the red numbers at the bottom means the final probabilities of each pixel merged into the two objects on the top level of L=3. Taking the pixel B1 as an example, there are two merging path from B1 to A3 (B1->A2->A3 and B1->B2->A3). According to Eq. (4-3), the probability of B1 merged into A3 is equal to 0.8×1+0.2×0.8=0.96. There is only one merging path from B1 to B3 (B1->B2->B3), therefore the probability of B1 merged into B3 is equal to 0.2×0.2=0.04. As shown in Fig. 4.3, the final probabilities of pixel B1 merged into the objects A3 and B3 are 0.96 and 0.04 respectively.

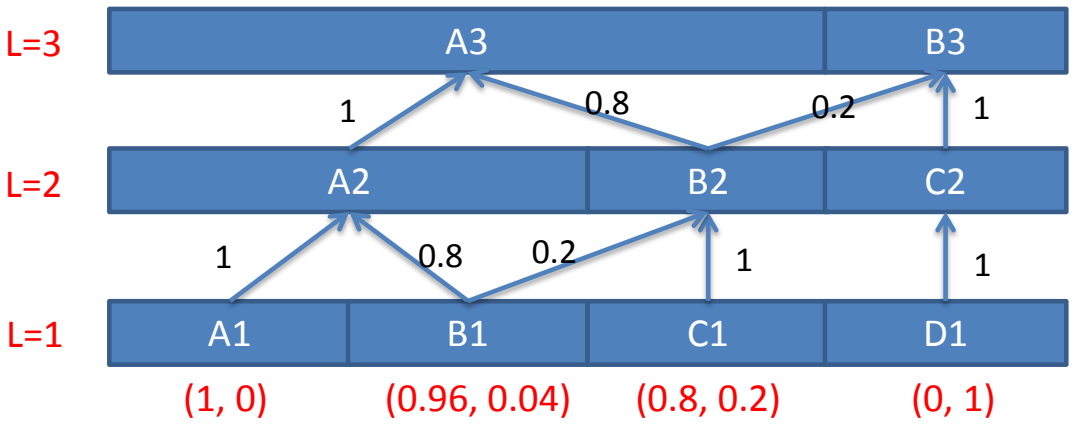

Fig. 4.3 Illustration of the summation of the probabilities on the merging paths

Finally, we could get the final probability of each pixel merged into each object on the top level of segmented images. If the probability of the pixel merged into its father object is higher, the merging process for this pixel is more reliable and with lower uncertainty. Therefore, the probabilities produced by the soft segmentation model can reflect the uncertainty in the merging procedure.

4.4 Case Study

4.4.1 Data and Study Area

A case study was conducted on a subset of an IKONOS image acquired in Beijing on 2001-04-26 (Fig. 4.4). This area locates in the center of this city and the main land cover objects include building, road, vegetation patch, river and bared playground. The sizes of these land cover objects are usually larger than the spatial resolution of the IKONOS image (4 meter). Therefore, the object based analysis method is more suitable for processing this image than the pixel based method.

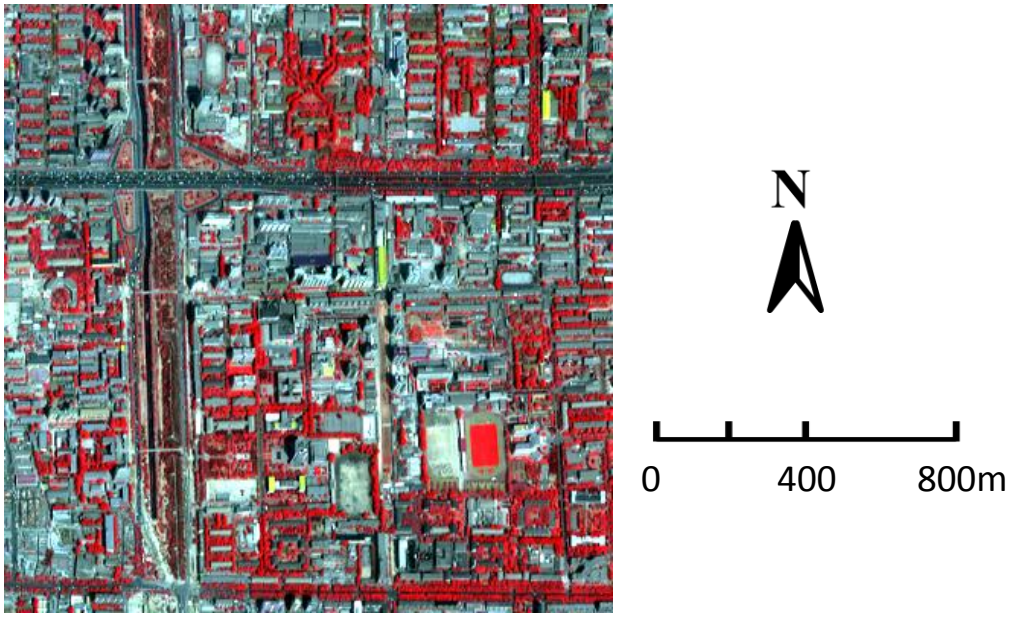

Fig. 4.4 IKONOS image in Beijing

4.4.2 Multi-resolution Segmentation

The commercial software, eCognition 8.0, was used for conducting the image segmentation. Segmented images on six levels with scale parameter *L*=5, 10, 15, 20, 25, and 30 were acquired. Fig. 4.5 shows the segmented images on the level of *L*=10, 20 and 30. As the *L* increases, the size of objects becomes larger and more detail information was removed.

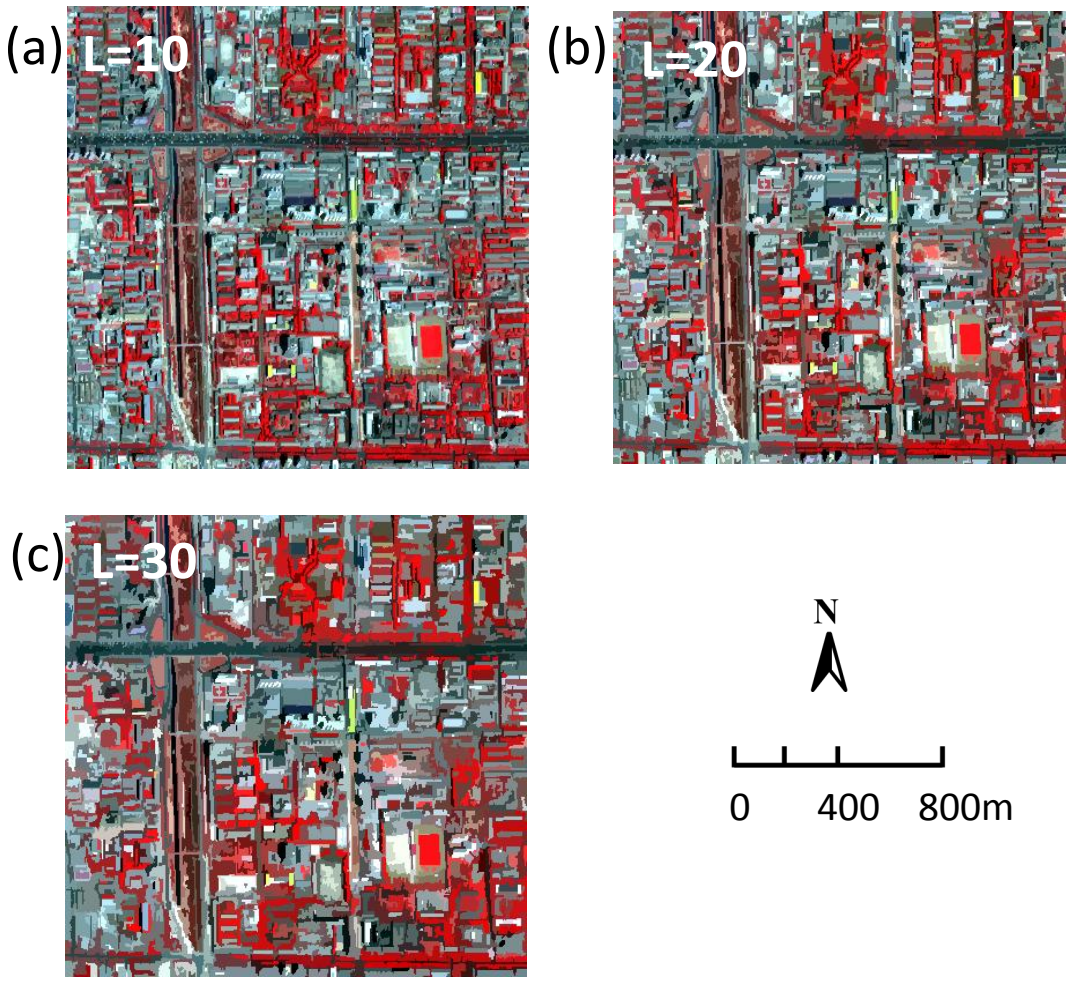

Fig. 4.5 Segmented images on different scale levels (a. *L*=10; b. *L*=20; c; *L*=30)

4.4.3 Result of Soft Segmentation Model

Based on the multi-resolution segmented images, soft segmentation result was acquired by the proposed soft segmentation model. Fig. 4.6 shows the probability of each pixel merged into its father object on top level of *L*=30. The brighter object is with higher reliability. A detail example is shown in Fig. 4.7. The object in the red polygon (Fig. 4.7a) corresponds to a vegetation patch which is clearly different from its surrounding objects (Fig. 4.7c). As shown in Fig. 4.7 (e), the pixels in the red

polygon have high probability of being merged into this object while the pixels outside the red polygon have very low probability of being merged into this object. Therefore, the red object is highly reliable. In contrast, the object in green polygon (Fig. 4.7a) does not correspond to a clear object, instead covers several land cover types including road, building roofs and trees (Fig. 4.7c). As shown in Fig. 4.7 (d), the pixels inside and outside the green polygon do not have much difference on the probability of being merged into this object. Therefore, the green object is with low reliability. Moreover, mixed pixels in the border can be also reflected in the probability image. As a profile of probability shown in Fig. 4.7 (f), For the pixels in the border of the red object, the probability of being merged into the red object decreases step by step from inside the object to outside the object, which is consistent with the characteristics of mixed pixels.

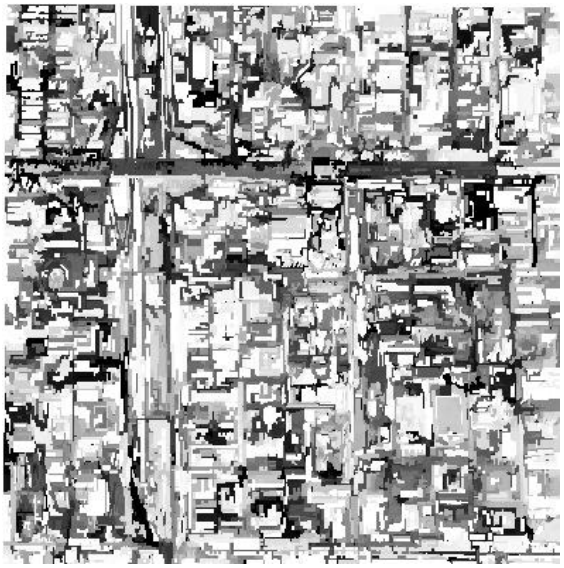

Fig. 4.6 Image of the probability of each pixel merged into its father object on the top level

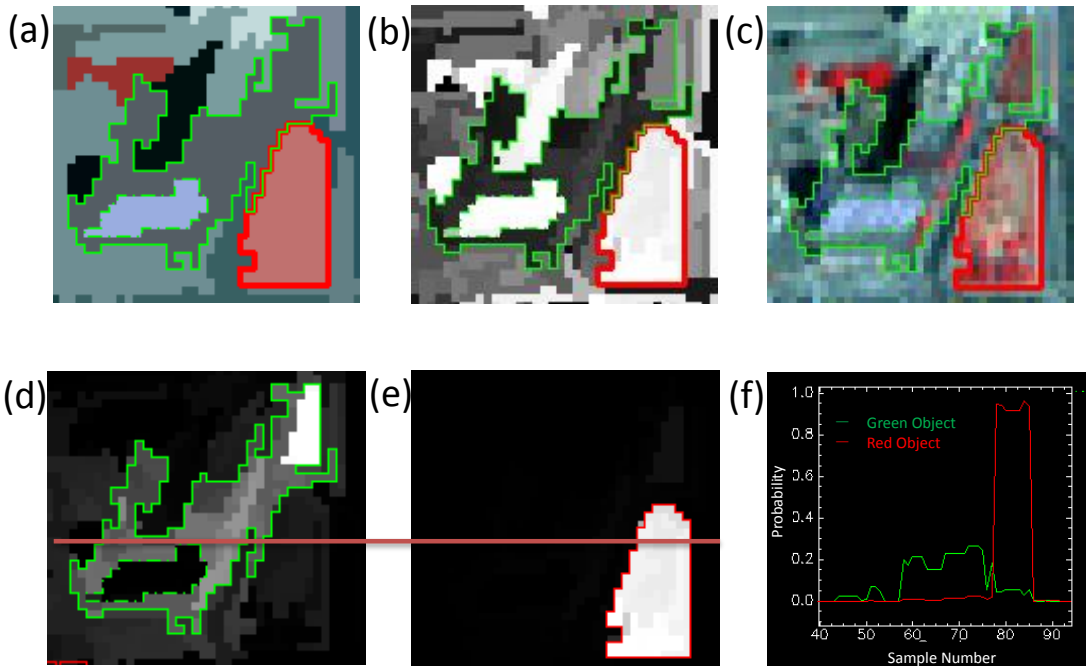

Fig. 4.7 A detail example of soft segmented result (a. hard segmented image; b. image of the probability of each pixel merged into its father object; c. original image; d. image of probability of each pixel merged into the green object; e. image of probability of each pixel merged into the red object; f. The probabilities of being merged into the green object and red object for the pixels on the red profile across fig. d and e)

4.5 Discussion and Conclusion

In this chapter, a soft segmentation model was proposed to describe the uncertainty in the multi-resolution segmentation procedure in eCognition. When the sub-objects are merged into the super-objects on the higher level, the probabilities of

being merged into different objects are calculated. Therefore, the uncertainty in the merging procedure is considered.

A case study of IKONOS image was conducted, and the result shows that the soft segmented image can represent the reliability of the object to some extent. The pixels in the object which corresponds to a pure land cover are with high probability of being merged into their father object. In contrast, the pixels in the object which covers several land covers are with low probability of being merged into their father object. Moreover, the mixed pixels in the border between objects can be also reflected in the soft segmentation result. These results indicate that the soft segmentation model can bring reasonable information of uncertainty, which is meaningful for understanding the reliability of the object based image analysis.

As a beginning attempt to quantitatively describe the uncertainty in image segmentation, there are limitations in the proposed soft segmentation model. In the hard image segmentation, both spectral information and shape information of the objects are considered. However, the proposed soft segmentation model only considers the spectral information, which cannot reflect all the uncertainties in the segmentation. Spectral, shape and textural information need to be considered in the future research.

CHAPTER 5

Scale Effect of Vegetation Index Based Spatial Sharpening for Thermal Imagery: A Simulation Study by ASTER Data

5.1 Introduction

Thermal infrared (TIR) band imagery has been widely applied in the studies on urban heat island effect exploration, evapotranspiration estimation and drought monitoring (Kato and Yamaguchi, 2005; Loheide li and Gorelick, 2005; Kafle and Yamaguchi, 2009; Shakya and Yamaguchi, 2010). Unfortunately, the spatial resolution of TIR bands of remote sensors is usually coarser than that of visible-near infrared (VNIR) bands, which limits its more precise application. Therefore, several techniques have been developed for sharpening TIR imagery by using VNIR bands (Kustas et al., 2003; Tonooka, 2005; Liu and Pu, 2008; Jing and Cheng, 2010; Dominguez et al., 2011; Zhan et al., 2011; Yang et al., 2011). Among them, vegetation index based spatial sharpening methods were intensively studied because of the simple and effective principle, the negative correlation between vegetation index and surface temperature (*T*) (Kustas et al., 2003; Agam et al., 2007a; Agam et al., 2007b; Yang et al., 2010; Merlin et al., 2010).

The most representative method is TsHARP, which was originally proposed by Kustas et al. (2003) and refined by Agam et al. (2007a). TsHARP disaggregates *T* image to the spatial resolution of VNIR band using empirically derived relationship

between NDVI and *T*. This method is valid based on the assumption that the relationship of NDVI -*T* is scale independent. Marceau and Hay (1999) proposed that there are two aspects of scale in remotely sensed imagery: grain and extent. Grain corresponds to the spatial resolution, and extent corresponds to the spatial extent of the study area. However, previous studies only focused on spatial resolution issue but ignored the spatial extent issue. It was shown that the relationship established on coarse resolution will not change (or change slightly) on fine resolution in the previous studies (Agam et al., 2007a). However, only resolution independence cannot ensure the effectiveness of the vegetation index based spatial sharpening method. The spatial extent is also a key factor affecting the NDVI-*T* relationship. Therefore, in this study, we investigated NDVI-*T* relationships on different spatial extents and spatial resolutions. And then we modified TsHARP method by considering the spatial extent effect and tested it in a simulation study using ASTER data.

5.2 Method

5.2.1 TsHARP

TsHARP (Agam et al., 2007a) firstly performs least-squares regression between *T* and NDVI on the coarse thermal resolution ($NDVI_{,low}$).

$$\hat{T}(\mathrm{NDVI}_{\mathrm{low}}) = f(\mathrm{NDVI}_{\mathrm{low}}), \tag{5-1}$$

As suggested by Agam et al. (2007a), following function was employed

$$f(\mathrm{NDVI}) = a(1-\mathrm{NDVI})^{0.625} - b \tag{5-2}$$

where *a* is regressed slope and *b* is constant term. And then this regression relationship is applied to the NDVI at their finer resolution ($NDVI_{high}$). After that, the divergence of the retrieved temperatures from the observed temperature field is assessed at the coarser resolution

$$\Delta\hat{T}_{low} = T_{low} - a \times (1 - NDVI_{low})^{0.625} - b \quad . \tag{5-3}$$

This coarse-resolution residual field is then added back into the sharpened map

$$\begin{aligned} \hat{T}_{high} &= a \times (1 - NDVI_{high})^{0.625} + b + \Delta\hat{T}_{low} \\ &= T_{low} + a \times \left[(1 - NDVI_{high})^{0.625} - (1 - NDVI_{low})^{0.625} \right] \end{aligned} \tag{5-4}$$

It can be seen that regressed slope (*a*) is the key parameter for the sharpening result.

5.2.2 Study on Scale Effect of NDVI -T Relationship

(1) NDVI -T Relationship on Different Spatial Resolutions

Because the term of $(1\text{-}NDVI_{low})^{0.625}$ is regarded to be linearly correlated with vegetation fraction (Agam et al., 2007a), we resampled the images of $(1\text{-}NDVI_{low})^{0.625}$ to different spatial resolution by linear aggregations. Also, *T* images were resampled to different spatial resolutions by linear aggregation. Here, nonlinear relationship between temperature and emissivity was not considered because different temperature aggregation methods produce low differences (Liu et al., 2006). Then, the regressed slopes of $(1\text{-}NDVI_{low})^{0.625}$-*T* relationship on different spatial resolutions were investigated.

(2) NDVI -T Relationship on Different Spatial Extents

Spatial extent is another important aspect of the scale effect, but was neglected in the previous studies. In order to establish the NDVI-*T* relationship on a certain spatial extent, the larger scale of spatial variance of NDVI and *T* should be firstly removed. The large scale of spatial variance corresponds to the variance of low-frequency component of an image. Therefore, we introduced a simple high-pass filter to remove the large scale of spatial variance.

The calculation process of high-pass filtering is illustrated in Fig. 5.1. Supposing that we try to study the image on the spatial extent of *m* pixels, the original image is firstly divided into $N/(m \times m)$ windows, where each window has $m \times m$ pixels and *N* is the number of pixels in the whole image. Secondly, an averaged image is acquired by averaging the values of the pixels in each window. Then, high-frequency component image corresponding to *m*-pixel spatial extent is derived by subtracting the original image with the averaged image. The regression analysis is then conducted on the high-frequency component image of $(1\text{-}NDVI_{low})^{0.625}$ and *T*. The regressed slope on the spatial extent of *m* pixels can be finally acquired. Through this method, regressed slopes on the different spatial extents were investigated.

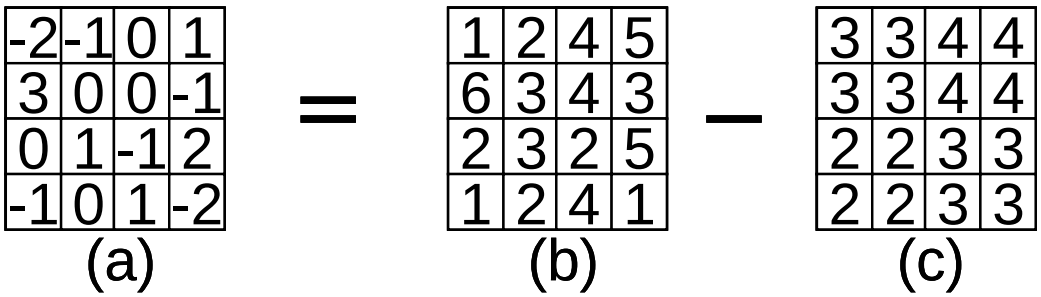

Fig. 5.1 Illustration of high-pass filtering (a. high-frequency component image; b. original image; c. averaged image)

5.2.3 Modified TsHARP

Sharpening *T* image is equal to retrieving the high frequency component image of *T* on the spatial extent which is equal to a thermal pixel. Unfortunately, regressed slope on such scale cannot be acquired without *T* image with fine resolution. However, we can establish the NDVI-*T* relationship on the minimum available spatial extent (2×2 pixels of thermal-infrared image) instead of the whole image. Therefore, we replaced the regressed slope on the whole image in Eq. (5-4) with that on the 2×2 thermal pixels (a_{local})

$$\hat{T}_{\text{high}} = T_{\text{low}} + a_{\text{local}} \times \left[(1 - \text{NDVI}_{\text{high}})^{0.625} - (1 - \text{NDVI}_{\text{low}})^{0.625} \right] \quad (5\text{-}5)$$

It is noticed that a_{local} is calculated based on the whole high frequency component images, where the sample size is equal to that of original TsHARP, and a unique a_{local} is derived. The modified method considers the factor of spatial extent and is expected to acquire more accurate sharpening result.

5.3 Simulation Study

5.3.1 Study Area and Data

Two subsets of ASTER images (256×256 pixels with 90 m resolution) were employed for our study. One subset image of ASTER (Fig. 5.2a) was acquired in Inner Mongolia, China (44.6N, 116.0E), on the date of July 16, 2010. Grassland is the dominant landscape in this semi-arid area, where water is one of the most important limiting factors for vegetation status (Cao et al., 2009). Another subset image of

ASTER (Fig. 5.2c) was acquired in Haihe River Basin, China (38.3N, 114.7E), on the date of April 26, 2002. Irrigated cropland is the dominated landscape in this area. The atmospheric corrected VNIR band reflectance and surface temperature (*T*) were produced by GEO Grid (AIST, 2007). In order to be consistent with TIR data, the spatial resolution of VNIR band was also resampled to 90 m resolution by linear aggregation. As shown in Fig. 5.3, there are negative correlations between NDVI and *T* for both of the two landscapes.

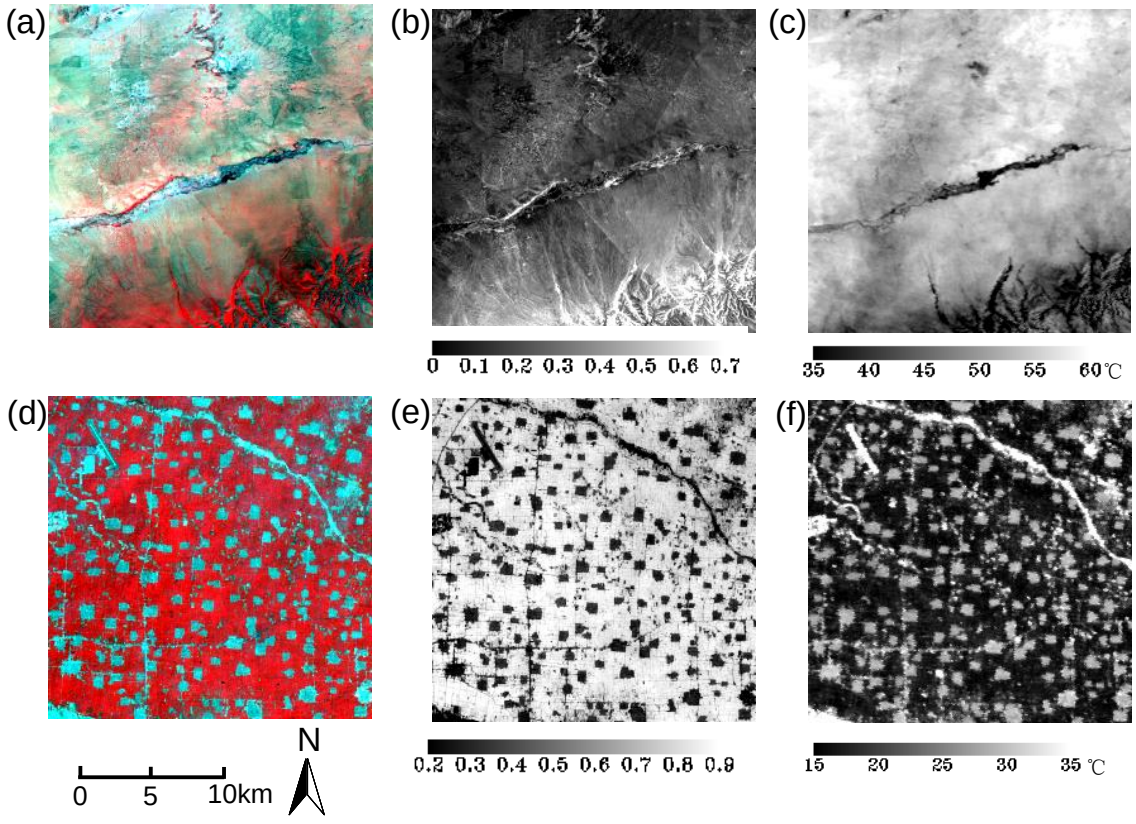

Fig. 5.2 ASTER data (a. VNIR band of grassland; b. NDVI of grassland; c. Surface temperature of grassland; d. VNIR band of cropland; e. NDVI of cropland; f. Surface temperature of cropland)

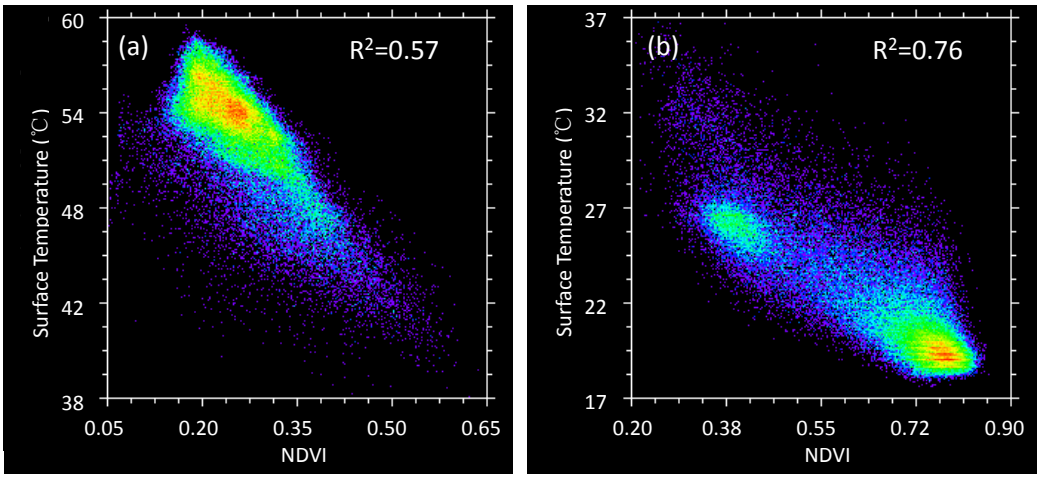

Fig. 5.3 Scatterplot of NDVI and *T* (a. grassland; b. cropland), the color from blue to red corresponds to the density from low to high

5.3.2 Scale Effect of NDVI-T Relationship

We investigated the NDVI-*T* relationship on the spatial resolution of 90 m, 180 m, 360 m, 720 m, 1440 m, and 2880 m, and on the spatial extent of 180 m, 360 m, 720 m, 1440 m, 2880 m, 5760 m, 11520 m, and 23040 m, which corresponded to 2, 4, 8, 16, 32, 64, 128, and 256 pixels, respectively.

Fig. 5.4(a) shows the regressed slopes on different spatial extents and spatial resolutions for the grassland. As shown in Fig. 5.4(a), the regressed slope increases when the spatial resolution becomes coarser, and also significantly increases with increasing of spatial extent. The regressed slope on spatial extent of 23040 m is up to three times larger than that on spatial extent of 180 m. However, when the spatial

extent becomes larger, the regressed slope becomes less sensitive to the change of spatial resolution and spatial extent.

Fig. 5.4(b) shows the regressed slopes on different spatial extents and spatial resolutions for the cropland. The regressed slope increases dramatically with increasing of spatial extent before it comes to 720 m, but becomes stable (or slightly decreases) when it is larger than 720 m. But in the case of 2880 m spatial resolution, the regressed slope decreases largely with increasing of spatial extent.

In summary, NDVI-*T* relationship is largely affected by spatial extent. The scale effect is complex, varying from case to case.

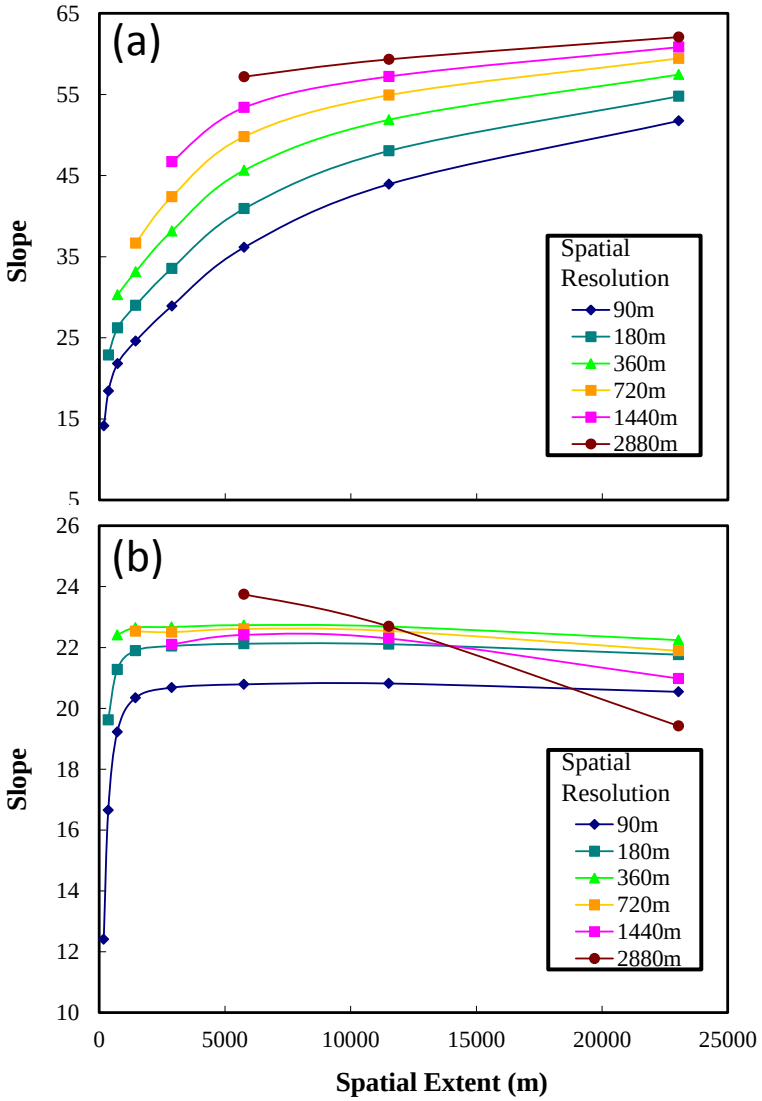

Fig. 5.4 Regressed slopes on different spatial extents and spatial resolutions (a. grassland; b. cropland)

5.3.3 Sharpening Experiments

In order to validate our modified method, we simulated *T* images with 900 m resolution (Fig. 5.5a and Fig. 5.7a) by linearly averaging the *T* image with 90 m resolution. The *T* image with 900 m resolution and NDVI image with 90 m resolution

were then used for the spatial sharpening experiments, and the original *T* image with 90 m resolution was used for validation.

(1) Case of Grassland

For the grassland, the new method estimated the regressed slope of $(1\text{-}NDVI_{low})^{0.625}$-*T* as 32.9, while the original TsHARP estimated it as 54.3, which obviously exaggerated the role of NDVI. Therefore, as shown in Fig. 5.5, the sharpened *T* image by the new method is smoother than that by TsHARP. In order to investigate how the regressed slope determines the sharpening accuracy, we sharpened the *T* image using different slopes ranging from 0 to 60; meanwhile, root mean square error (RMSE) and square of correlation coefficient (R square) were calculated for accuracy assessment. As shown in Fig. 5.6, the best value of slope is around 23.0, which is much more approximate to the regressed slope estimated by the new method than that estimated by the TsHARP. The accuracy of TsHARP is lower than that of new method, and even lower than that of uniform disaggregation which employs a zero value of slope. It indicates that TsHARP is not suitable for grassland.

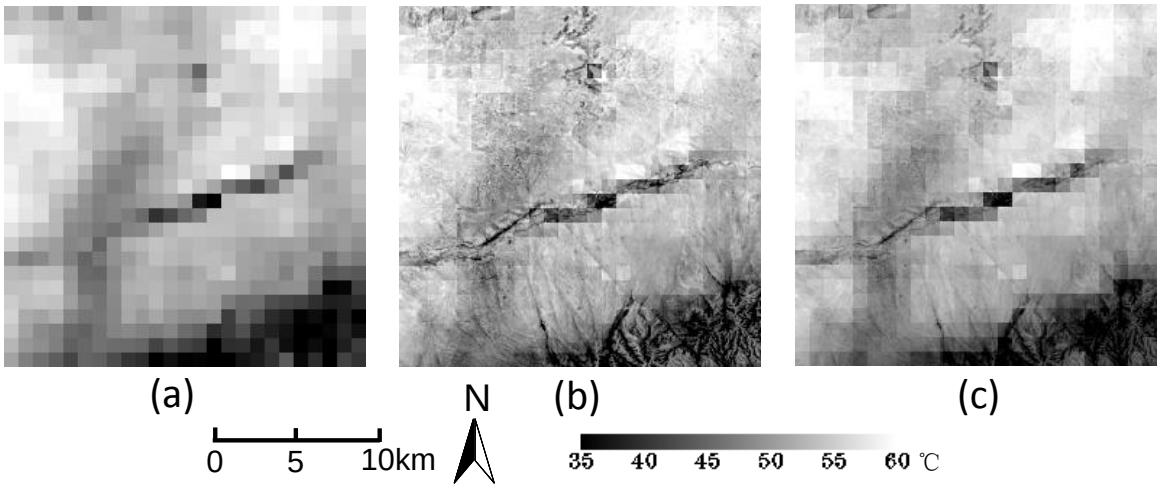

Fig. 5.5 Surface temperature (*T*) image of grassland (a. with 900 m resolution; b. sharpened by TsHARP; c. sharpened by new method)

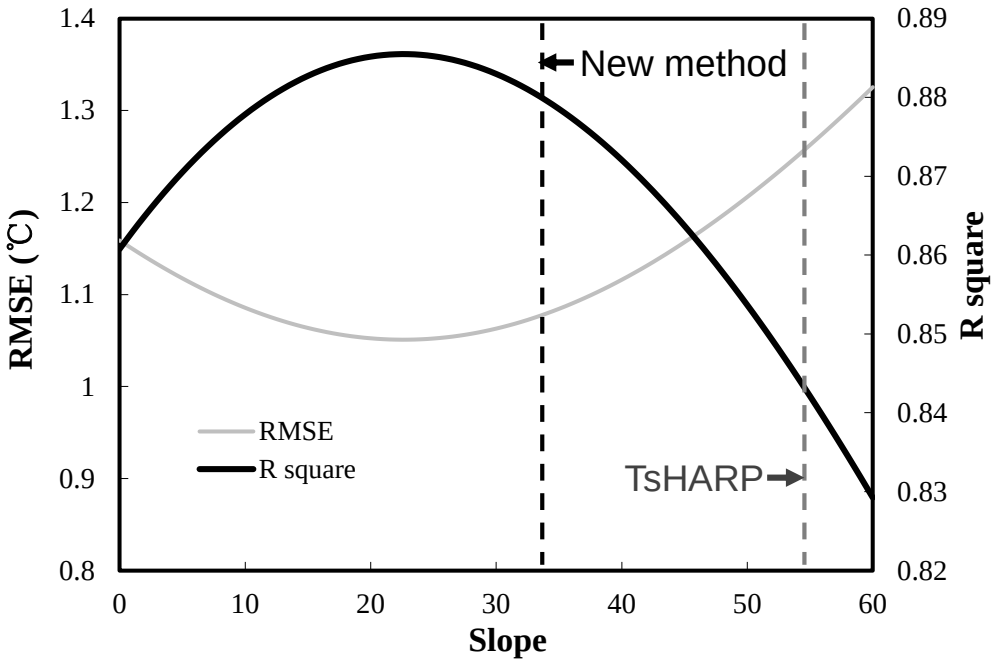

Fig. 5.6 Relationship between the sharpening accuracy and regressed slope in grassland

(2) Case of Cropland

For the cropland, the new method estimated the regressed slope of $(1\text{-}NDVI_{low})^{0.625}$-*T* as 23.4, and the original TsHARP estimated it as 21.9. Therefore, the two methods produced very similar sharpening result (Fig. 5.7). Similarly, we sharpened the *T* image using regressed slopes ranging from 0 to 60. As shown in Fig. 5.8, the best value of sharpening slope is around 20.0, which is approximate to the regressed slopes estimated by the two methods. Both of two methods performs much better than uniform disaggregation. The reason for the similar results by two different methods is that regressed slope keeps stable when the spatial extent is larger than 720 m, therefore, the new method cannot show its advantage. In summary, both of the TsHARP and new method are suitable for cropland.

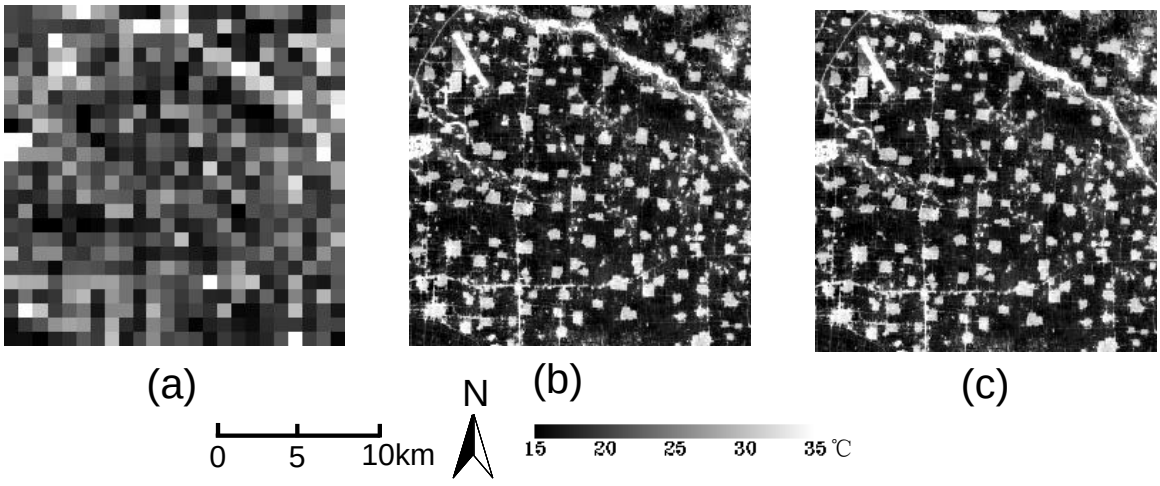

Fig. 5.7 Surface temperature (*T*) image of cropland (a. with 900 m resolution; b. sharpened by TsHARP; c. sharpened by new method)

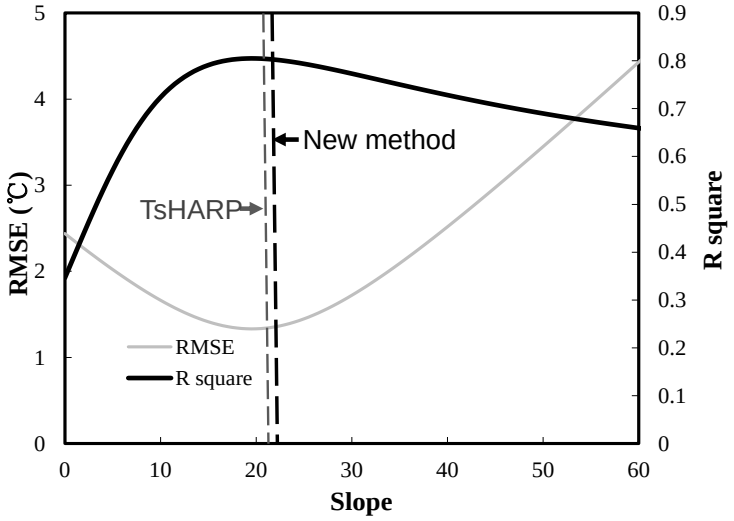

Fig. 5.8 Relationship between the sharpening accuracy and regressed slope in cropland

(3) Sharpening from Different Source Resolutions to Different Target Resolutions

Additionally, we conducted the experiments of spatial sharpening from different source resolutions (sharpening to 90 m from 900 m, 720 m, 360 m, and 180 m) and sharpening to different target resolutions (sharpening from 900 m to 450 m, 180 m, and 90 m). The sharpening accuracies were compared in Fig. 5.8. Similar to the previous study (Agam et al., 2007), the sharpening accuracy is higher when the source resolution and target resolution is closer. For the grassland, the new method acquired the highest accuracy, while TsHARP acquired the lowest accuracy, even lower than uniform disaggregation in most cases (Fig. 5.9 a and b). For the cropland, TsHARP performed slightly better than the new method except for the case of sharpening from 180 m to 90 m (Fig. 5.9 c and d). In this case, the new method performed better

because the effect of spatial size for cropland becomes obvious when the spatial size is less than 360 m.

In summary, both of the original TsHARP and new method are suitable for the cropland, while TsHARP could produce large error for the grassland.

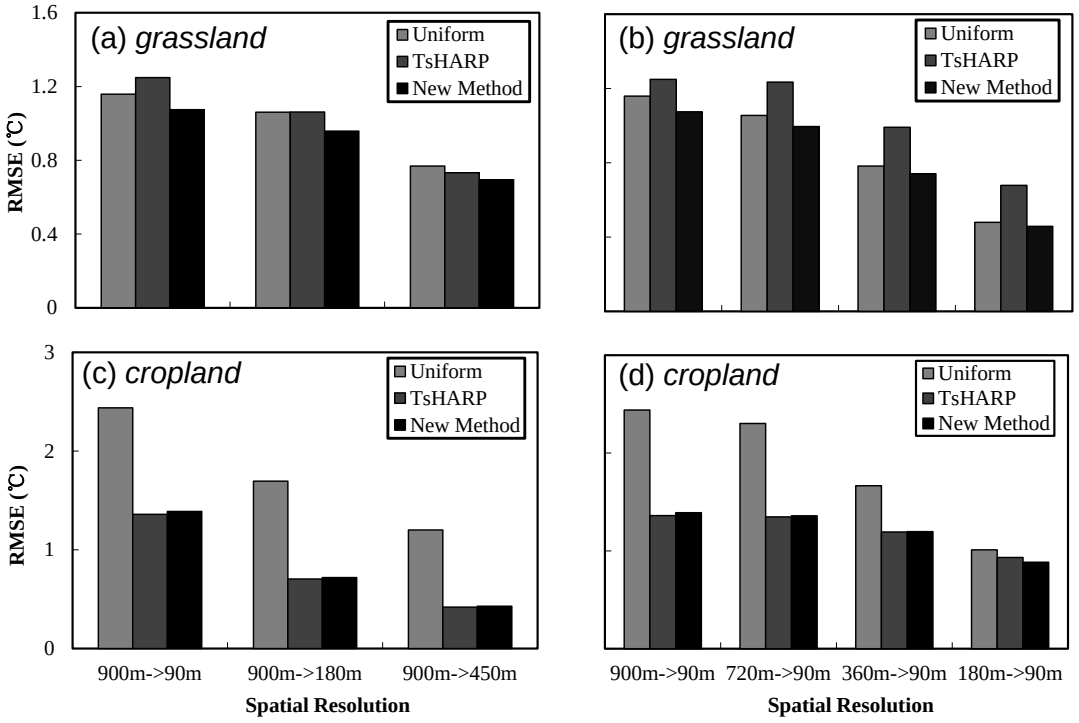

Fig. 5.9 Accuracies (RMSE) of sharpening from different source resolutions to different target resolutions (a. sharpening to 90 m from 900 m, 720 m, 360 m, and 180 m in grassland; b. sharpening from 900 m to 90 m, 180 m, and 450 m in grassland; c. sharpening to 90 m from 900 m, 720 m, 360 m, and 180 m in cropland; d. sharpening from 900 m to 90 m, 180 m, and 450 m in cropland)

5.4 Discussion

In this study, NDVI-*T* relationships established on different spatial extents were found to be largely different. The reason may be related to the positive correlation between NDVI and soil moisture. It is well known that soil moisture also affects the surface temperature largely. It is reasonable to assume that

$$T = a \cdot (1 - \mathrm{NDVI})^{0.625} + a_{\mathrm{m}} \cdot Moisture, \tag{5-6}$$

where a_{m} is the slope for moisture. Since NDVI is somehow positively correlated with soil moisture, when T is regressed with only $(1\text{-}\mathrm{NDVI}_{\mathrm{low}})^{0.625}$, the regressed slope becomes (for convenience, we assume the data is standardized)

$$\hat{a} = a + a_{\mathrm{m}} \cdot r\left[(1 - \mathrm{NDVI})^{0.625},\ \mathrm{Moisture}\right], \tag{5-7}$$

where $r[(1\text{-}\mathrm{NDVI}_{\mathrm{low}})^{0.625},$ Moisture] is the correlation coefficient between $(1\text{-}\mathrm{NDVI}_{\mathrm{low}})^{0.625}$ and soil moisture. Hence, $\hat{a}$ becomes smaller when the correlation between NDVI and Moisture becomes weaker. In the grassland, there is a triangular in NDVI-*T* scatterplot (Fig. 5.3a). It implies that the spatial patterns of soil moisture and NDVI are not matched well because the soil moisture varies more smoothly than NDVI in the spatial pattern. As a result, when the spatial extent decreases, the correlation between NDVI and moisture becomes weaker and $\hat{a}$ decreases correspondingly. While in the irrigated cropland, there is a much better correlation between NDVI and *T* (Fig. 5.3b). The reason may be that soil moisture is also correlated well with NDVI in the cropland. Such explanation is reasonable because irrigation is only conducted on the vegetated cropland. Therefore, the spatial pattern

of moisture is not smoother than that of NDVI in large scale. That could explain why the regressed slope becomes stable when the spatial extent is larger than 720 m. Such difference in the scale effect of NDVI-*T* relationship leads to the different performance of TsHARP in grassland and cropland. Our result suggests that TsHARP is more suitable in cropland, which is similar with the previous study (Agam et al., 2007b), where a worse performance of TsHARP was found in natural land cover compared with agricultural land cover.

The above explanation is reasonable for this case study. For the other cases, the physical reason of the scale effect might be different. And also the scale effect does not only exist in NDVI-*T* relationship, but possibly can be found in the relationship of other land surface parameters as well. We suggest that spatial extent is also a very important aspect of scale effect other than spatial resolution, and should be considered in the related studies.

5.5 Conclusion

Our study shows that the spatial extent is an important scale factor affecting the NDVI-*T* relationship except of spatial resolution, but was largely neglected in the previous studies. Previous spatial sharpening methods for thermal imagery which apply NDVI-*T* relationship established on the whole image to the small spatial extent (thermal resolution) may produce a large error. We modified TsHARP by establishing the NDVI-*T* relationship on the minimum available spatial extent. The simulation

study shows that the new method can acquire good sharpening accuracy for both of the grassland and cropland, while the original TsHARP method produced a large error for grassland. Therefore, we can conclude that the modified method is more robust than the original TsHARP.

CHAPTER 6

Discussion and Conclusion

6.1 Discussion

Spatial features are valuable information in remotely sensed images. Although many mathematic tools are available for extracting the spatial features, they were originally designed for general images without much consideration of the geographic characteristics in remotely sensed image. Therefore, they were only used for land cover classification in the previous studies. This thesis extended the application of spatial features in the fields of classification accuracy assessment, automated land cover updating, uncertainty in image segmentation, and spatial sharpening for thermal images. The mathematic tools for spatial feature extracting were revised by considering the particular geographic characteristics including the landscape pattern, mixed pixels, and scale effect. Therefore, the methodologies or models in those fields were significantly improved compared with previous studies.

There are still many other fields where spatial features were rarely considered. Till now, most quantitative remote sensing models which are used for retrieving the biophysical parameters (e.g. LAI, biomass, LUE, evapotranspiration, etc.) are sub-pixel models, where the scale of geographic elements is assumed smaller than the spatial resolution and spatial features were neglected. As the spatial resolution of

remotely sensed image increases, this assumption collapses and the spatial features become more important and should be considered more in developing such models.

In this thesis, the mathematical tools for extracting spatial features were categorized into three types: moving-window based, object based and image based methods. However, it should be noticed that there are other methods which are difficult to be categorized into any kind of these three methods. For example, the wavelet transformation which is localized in both spatial domain and frequency domain can be regarded as a method between moving-window based and image based. The seed-growing algorithm which considers the adjacent pixels in an adaptive window can be regarded as a method between moving-window based and object based.

As there is a need of considering the spatial features in quantitative remote sensing models, meanwhile many mathematical tools for extracting spatial features are available, further combing them together will be my future research.

6.2 Conclusion

In this thesis, better methodologies and models in four fields were achieved by considering spatial features.

(1) The proposed Weighted Misclassification Rate (WMR) which can predict the Landscape Pattern Index (LPI) error induced by classification error is an important supplement to traditional accuracy assessment indices.

(2) The proposed integrated, automated updating approach for land cover mapping can produce land cover maps efficiently. Compared with previous methods, multi-source remotely sensed data can be combined together and human interactions are not required in the proposed approach.

(3) The soft segmentation model is a beginning attempt to quantitatively describe the uncertainty in the object based methods as the uncertainty was largely neglected in the previous studies.

(4) The improved vegetation-index-based spatial sharpening method for thermal imagery which considers the scale effect performs more robustly than the original method.

REFERENCES

Addink E. A., de Jong S. M., and Pebesma E. J., (2007). The importance of scale in object based mapping of vegetation parameters with hyper spectral imagery. *Photogrammetric Engineering and remote sensing*, 73(8), 905-912.

Agam N., Kustas W. P., Anderson M. C., Li F., and Neale C. M. U., (2007a). A vegetation index based technique for spatial sharpening of thermal imagery. *Remote Sensing of Environment*, 107 (4), 545-558.

Agam N., Kutas W. P., Anderson M. C., Li F., and Colaizzi P. D., (2007b). Utility of thermal sharpening over Texas high plains irrigated agricultural fields. *Journal of Geophysical Research*, 112, D19110.

AIST, (2007). Feature: GEO Grid innovation in Global Earth Observation. *AIST Today International Edition*, Autumn, 26, 2-11.

Aitkenhead M. J., and Aalders I. H., (2011). Automating land cover mapping of Scotland using expert system and knowledge integration methods. *Remote Sensing of Environment*, 115 (5), 1285-1295.

Arino O., Bicheron P., Achard F., Latham J., Witt R., and Weber J. L., (2008). GLOBCOVER: the most detailed portrait of the earth. *ESA Bulletin-European Space Agency*, 136, 24-31.

Baatz M., (2000). Multiresolution Segmentation: an optimization approach for high quality multi-scale image segmentation. Journal of Photogrammetry and Remote Sensing, 58 (3-4), 12-23.

Bannari A., Morin D., Bonn F., and Hute A. R., (1995). A review of vegetation indices. *Remote Sensing Reviews*, 13(1-2), 95-120.

Bartholomé E., and Belward A. S., (2005). GLC2000: A new approach to global land cover mapping from Earth Observation data. *International Journal of Remote Sensing*, 26 (9), 1959-1977.

Besag J., (1986). On the statistical analysis of dirty pictures. *Journal of Royal Statistical Society, Series B (Methodological)*, 48 (3), 259-302.

Blaschke T., (2010). Object based image analysis for remote sensing. *ISPRS Journal of Photogrammetry and Remote Sensing* 65 (1), 2-16.

Bruzzone L. and Prieto D. F., (2000). Automatic analysis of the difference image for unsupervised change detection. *IEEE Transactions on Geoscience and Remote Sensing* 38 (3), 1171-1182.

Canty M. J., (2006). Image analysis, classification and change detection in remote sensing with algorithms for ENVI/IDL. Taylor & Francis, CRC Press.

Cao X., Chen J., Matsushita B., Imura H., and Wang L., (2009). An automatic method for burn scar mapping using support vector machines. *International Journal of Remote Sensing*, 30 (3), 577-594.

Castellana L., D'Addabbo A., and Pasquariello G., (2007). A composed supervised/ unsupervised approach to improve change detection from remote sensing. *Pattern Recognition Letters*, 28(4), 405-413.

Chen J., Chen X., Cui X., and Chen J., (2011). Change vector analysis in posterior probability space: a new method for land cover change detection. *IEEE Geoscience and remote sensing letters*, 8 (2), 317-321.

Chen J., Gong P., He C., Pu R., and Shi P., (2003). Land-use/land-cover change detection using improved change-vector analysis. *Photogrammetric Engineering and Remote Sensing*, 69 (4), 369-379.

Chen J., Shao Y., and Zhu B., (2004). Destriping CMODIS Based on FIR Method. *Journal of Remote Sensing*. 8(3), 227-233. (In Chinese)

Chen J., Zhu X., Imura H, and Chen X., (2010). Consistency of accuracy assessment indices for soft classification. *ISPRS Journal of Photogrammetry and Remote Sensing*, 65, 156-164.

Comer M., and Delp E., (1999). Morphological operations for color image processing. *Journal of Electronic Imaging*, vol. 8, pp. 279–289, July

Definiens, (2009). eCognition Developer 8 - User Guide. Definiens A. G., Munchen, Germany.

Dey V., Zhang Y., and Zhong Y., (2010). A review on image segmentation techniques with remote sensing perspective. *ISPRS TC VII Symposium – 100 Years ISPRS*, Vienna, Australia, XXXVIII (Part 7A), 31-42.

Dixon B., and Candade N., (2007). Multispectral land use classification using neural networks and support vector machine: one or the other, or both? *International Journal of Remote Sensing*, 29 (4), 1185-1206.

Dominguez A., Kleissl J., Luvall J. C., and Rickman D. L., (2011). High-resolution urban thermal sharpener (HUTS). *Remote Sensing of Environment*, 115 (7), 1772-1780.

Foody G. M., (2002). Status of land cover classification accuracy assessment. *Remote Sensing of Environment*, 80, 185-201.

Franklin S. E., and Wulder M. A., (2002). Remote sensing methods in medium spatial resolution satellite data land cover classification of large areas. *Progress in Physical Geography*, 26 (2), 173-205.

Friedl M. A., McIver D. K., Hodges J. C. F., Zhang X. Y., Muchoney D., Strahler A. H., Woodcock C. E., Gopal , S., Schneider A., Cooper A., Baccini A., Gao, F., and Schaaf C., (2002). Global land cover mapping from MODIS: Algorithms and early results. *Remote Sensing of Environment*, 83(1-2), 287−302.

Guindon B., (1997). Computer-based aerial image understanding: a review and assessment of its application to planimetric information extraction from very high resolution satellite images. *Canadian Journal of Remote Sensing*, 23 (1), 38-47.

Hansen M. C., Defries R. S., Townshend J. R. G., and Sohlberg R., (2000). Global land cover classification at 1 km spatial resolution using a classification forest approach. *International Journal of Remote Sensing*, 21 (6-7), 1331−1364.

Hansen M. C., and Reed B., (2000). A comparison of the IGBP DISCover and University of Maryland 1 km global land cover products. *International Journal of Remote Sensing*, 21 (6-7), 1365-1373.

Haralick R. M., and Shapiro L. G., (1985). Image segmentation techniques. *Computer Vision, Graphics and Image Processing*, 20 (2), 101-132.

Hess G. R., (1994). Pattern and error in landscape ecology: a commentary. *Landscape Ecology*, 9, 3-5.

Ho L. T. K., and Umitsu M., (2011). Micro-landform classification and flood hazard assessment of the Thu Bon alluvial plain, central Vietnam via an integrated method utilizing remotely sensed data. *Applied Geography*, 31 (3), 1082-1093.

Iwao K., Nishida K., Kinoshita T., and Yamagata Y., (2006). Validating land cover maps with degree confluence project information. *Geophysical Research Letters*, 33, L23404.

Jeon B. and Landgrebe D. A., (1991). Spatio-temporal contextual classification based on Markov random field model. *Proceedings of the International Geoscience and Remote Sensing Symposium*, June, 1819-1822.

Jing L., and Cheng Q., (2010). A technique based on non-linear transform and multivariate analysis to merge thermal infrared data and higher-resolution multispectral data. *International Journal of Remote Sensing*, 31 (24), 6459-6471.

Kafle H. K., and Yamaguchi Y., (2009). Effects of topography on the spatial distribution of evapotranspiration over a complex terrain using two-source energy balance model with ASTER data. *Hydrological Processes*, 23, 2295-2306.

Kaptué Tchuenté A. T., Roujean J. L., and de Jong S. M., (2011). Comparison and relative quality assessment of the GLC2000, GLOBCOVER, MODIS and ECOCLIMAP land cover data sets at the African continental scale. *International Journal of Applied Earth Observation and Geoinformation*, 13 (2), 207-219.

Kapur J. N., Sahoo P. K., and Wong A. K. C., (1985). A new method for gray level picture thresholding using the entropy of the histogram. *Computer Vision, Graphics, and Image Processing*, 29 (3), 273-285.

Kato S., and Yamaguchi Y., (2005). Analysis of urban heat-island effect using ASTER and ETM+ Data: Separation of anthropogenic heat discharge and natural heat radiation from sensible heat flux. *Remote Sensing of Environment*, 99 (1-2), 44-54.

Kohli P., and Torr P. H. S., (2007). Dynamic graph cuts for efficient inference in Markov Random Fields. *IEEE Transactions on Pattern Analysis and Machine Intelligence*, 29 (12), 2079-2088.

Kustas W. P., Norman J. M., Anderson M. C., and French A. N., (2003). Estimating subpixel surface temperatures and energy fluxes from the vegetation index-radiometric temperature relationship. *Remote Sensing of Environment*, 86 (4), 429-440.

Kuzera K., and Pontius Jr R.G., (2008). Importance of matrix construction for multiple-resolution categorical map comparison. *GIS and Remote Sensing*, 45, 249-274.

Langford W. T., Gerge S. E., Dietterich, T. G., and Cohen W., (2006). Map misclassification can cause large errors in landscape pattern indices: example from habitat fragmentation. *Ecosystems*, 9, 474-488.

Li X., He H. S., Bu R., Wen Q., Chang Y., Hu Y., and Li Y., (2005). The adequacy of different landscape metrics for various landscape patterns. *Pattern Recognition*, 38, 2626-2638.

Liang S. L., (2004), *Quantitative Remote Sensing of Land Surfaces*, NewYork: John Wiley and Sons, Inc.

Lillesand T. M., and Kiefer R. W., (2000). *Remote Sensing and Image Interpretation*, 4th, Wiley, New York.

Liu D., Maggi K., and Gong P., (2006). A spatial-temporal approach to monitoring forest disease spread using multi-temporal high spatial resolution imagery. *Remote Sensing of Environment*, 101 (2), 167-180.

Liu D., and Pu R., (2008). Downscaling thermal infrared radiance for subpixel land surface temperature retrieval. *Sensors*, 8 (4), 2695-2706.

Liu D., Song K., Townshend J. R. G., and Gong P., (2008). Using local transition probability models in Markov random fields for forest change detection. *Remote Sensing of Environment*, 112 (5), 2222-2231.

Liu Y., Hiyama Y., and Yamaguchi Y., (2006). Scaling of land surface temperature using satellite data: A case examination on ASTER and MODIS products over a heterogeneous terrain area. *Remote Sensing of Environment*, 105 (2), 115-128.

Loheide li S. P., and Gorelick S. M., (2005). A local-scale, high-resolution evapotranspiration mapping algorithm (ETMA) with hydroecological applications at riparian meadow restoration sites. *Remote Sensing of Environment*, 98 (2-3), 182-200.

Loveland T. R., Reed B. C., Brown J. F., Ohlen D. O., Zhu Z., Yang L., and Merchant J. W., (2000). Development of a global land cover characteristics database and IGBP DISCover from 1 km AVHRR data. *International Journal of Remote Sensing*, 21 (6-7), 1303-1330.

Lu D., Mausel P., Brondizio E., and Moran E., (2004). Change detection techniques. *International Journal of Remote Sensing*, 25 (12), 2365-2407.

Lu D., and Weng Q., (2007). A survey of image classification methods and techniques for improving classification performance. *International Journal of Remote Sensing*, 28 (5), 823-870.

Lucieer A., and Stein A., (2002). Existential uncertainty of spatial objects segmented from satellite sensor imagery. *IEEE Transactions on Geoscience and Remote Sensing*, 40 (11), 2518-2521.

Macleod D. R., and Congalton G. R., (1998). A quantitative comparison of change detection algorithms for monitoring eelgrass from remotely sensed data. *Photogrammetric Engineering and Remote Sensing*, 64 (3), 207-216.

Marceau D. J., and Hay G. J., (1999). Remote sensing contributions to the scale issue. *Canadian Journal of Remote Sensing*, 25 (4), 357-366.

Materka, A., and Strzelecki M. (1998). Texture analysis method – a review. *Technical University of Lodz, Institute of Electronics, COST B11 report*, Brussels.

Maxwell S. K., Nuckols J. R., Ward M. H., and Hoffer R. M., (2004). An automatic approach to mapping corn from Landsat imagery. *Computers and Electronics in Agriculture*, 43 (1), 43-54.

Mcgarigal K., Cushman S. A., Neel M. C., and Ene E., (2002). FRAGSTATS: Spatial Pattern Analysis Program for Categorical Maps. Available online at: www.umass.edu/landeco/research/fragstats/fragstats.html.

Merlin O., Duchemin B., Hagolle O., Jacob F., Coudert B., Chehbouni G., Dedieu G., Garatuza J., and Kerr Y., (2010). Disaggregation of MODIS surface temperature over an agricultural area using a time series of Formosat-2 images. *Remote Sensing of Environment*, 114 (11), 2500-2512.

Mountrakis G., Im J., and Ogole C., (2011). Support vector machines in remote sensing: A review. *ISPRS Journal of Photogrammetry and Remote Sensing*, 66 (3), 247-259.

Muñoz-Marí J., Bovolo F., Gómez-Chova L., Bruzzone L., and Camps-Valls G., (2010). Semisupervised One-Class Support Vector Machines for Classification of Remote Sensing Data. *IEEE Transactions on Geoscience and Remote Sensing*, 48 (8), 3188-3197.

Negi H. S., Kulkarni A. V., and Semwal B. S., (2009). Estimation of snow cover distribution in Beas basin, Indian Himalaya using satellite data and ground measurements. *Journal of Earth System Science*,118 (5), 525-538.

Newton A. C., Hill R. A., Echeverría C., Golicher D., Benayas J. M. R., Cayuela L., and Hinsley S. A., (2009). Remote sensing and the future of landscape ecology. *Progress in physical geography*, 33, 528-546.

Plaza A., Martinez P., Perez R., and Pala J., (2002). Spatial/spectral endmember extraction by multidimensional morphological operations. *IEEE Transactions on Geoscience and Remote Sensing*, 40(9), 2025-2041

Pontius Jr R. G., and Connors J., (2009). Range of categorical associations for comparison of maps with mixed pixels. *Photogrammetric Engineering & Remote Sensing*, 75, 963-969.

Richards J. A. and Jia X. (2006), *Remote Sensing Digital Image Analysis*, 3rd, Springer-Verlag.

Román M. O., and Coauthors, (2009): The MODIS (Collection V005) BRDF/albedo product: Assessment of spatial representativeness over forested landscapes. *Remote Sens. Environ.*, 113(11), 2476-2498.

Saadat H., Adamowski J., Bonnell R., Sharifi F., and Namdar M., (2011). Land use and land cover classification over a large area in Iran based on single date analysis of satellite imagery. *ISPRS Journal of Photogrammetry and Remote Sensing*, 66 (5), 608-619.

Saura S., and Martinez-Millan J., (2000). Landscape patterns simulation with a modified random clusters method. *Landscape Ecology*, 15, 661-678.

Schiewe J., (2002). Segmentation of high-resolution remotely sensed data – concepts, applications and problems. *Joint Commission IV Symposium: Geospatial Theory, Processing and Applications*, Ottawa, Canada, XXXIV (Part 4), 358-363.

Serra P., Pons X., and Sauru D., (2003). Post-classification change detection with data from different sensors: some accuracy consideration. *International Journal of Remote Sensing*, 24 (16), 3311-3340.

Shakya N., and Yamaguchi Y., (2010). Vegetation, water and thermal stress index for study of drought in Nepal and central northeastern India. *International Journal of Remote Sensing*, 31(4), 903-912.

Shao G., and Wu J., (2008). On the accuracy of landscape pattern analysis using remote sensing data. *Landscape Ecology*, 23, 505-511.

Soille P., and Pesaresi M. (2002) Advances in mathematical morphology applied to geoscience and remote sensing. *IEEE Transactions on Geoscience and Remote Sensing*, 40(9), 2042-2055.

Solberg A. H. S., Taxt T., and Jain A. K., (1996). A markov random field model for classification of multisource satellite imagery. *IEEE Transactions on Geoscience and Remote Sensing*, 34 (1), 100-113.

Su W., Li J., Chen Y., Liu Z., Zhang J., Low T. M., Suppiah I., and Hashim S. A. M. (2008). Texture and local spatial statistics for the object-oriented classification of urban areas using high resolution imagery. *International Journal of Remote Sensing*, 29(11), 3105-3117.

Sui H., Peng F., Xu C., Sun K., and Gong J., (2012). GPU-accelerated MRF segmentation algorithm for SAR images. *Computer and Geosciences*, in press.

Stehman S. V., (2009). Sampling designs for accuracy assessment of land cover. *International Journal of Remote Sensing*, 30, 5243-5272.

Szeliski R., Zabih R., Scharstein D., Veksler O., Kolmogorov V., Agarwala A., Tappen M., and Rother C., (2008). A comparative study of energy minimization methods for markov random fields with smoothness-based priors. *IEEE Transactions on Pattern Analysis and Machine Intelligence*, 30 (6), 1068-1080.

Tonooka H., (2005). Resolution enhancement of ASTER shortwave and thermal infrared bands based on spectral similarity. *Proceedings of SPIE,* 5657, 9-19.

Tralli D. M., Blom R. G., Zlotnicki V., Donnellan A., and Evans D. L., (2005). Satellite remote sensing of earthquake, volcano, flood, landslide and coastal inundation hazards. *ISPRS Journal of Photogrammetry and Remote Sensing*, 59(4), 185-198.

Turner M. G., (2005). Landscape Ecology: What is the state of the science? *Landscape Ecology*, 36, 319-344.

Turner B. L., Skole D., Sanderson S., Fischer G., Fresco L., and Leemans, R., (1995). Land-use and Land-cover Change Science/Research Plan, IGBP Report No. 35.

Weng Q., (2011). Advances in environmental remote sensing: sensors, algorithms and applications. CRC Press/Taylor and Francis: Boca Raton, FL, USA.

Wu C. S., (2003). Normalized spectral mixture analysis for monitoring urban composition using ETM plus imagery. *Remote Sensing of Environment*, 93, 480-492.

Woodcock C. E., and Strahler A. H., (1987). The factor of scale in remote-sensing. *Remote Sensing of Environment*, 21: 311-332.

Xian G., Collin H., and Fry J., (2009). Updating the 2001 National Land Cover Database land cover classification to 2006 by using Landsat imagery change detection methods. *Remote Sensing of Environment*, 113 (6), 1133-1147.

Xie Y. Sha Z. and Bai Y., (2010). Classifying historical remotely sensed imagery using a tempo-spatial feature evolution (T-SFE) model. *ISPRS Journal of Photogrammetry and Remote Sensing*, 65 (2), 182-190.

Yang G., Pu R., Zhao C., Huang W., and Wang J., (2011). Estimation of subpixel land surface temperature using and endmember index based technique: a case examination on ASTER and MODIS temperature products over a heterogeneous area. *Remote Sensing of Environment*, 115 (5), 1202-1219.

Yang H., Cong Z., Liu Z., and Lei Z., (2010). Estimating sub-pixel temperatures using the triangle algorithm. *International Journal of Remote Sensing*, 31 (23), 6047-6060.

Zhan Q., Molenaar M., Tempfli K., and Shi W., (2009). Quality assessment for geo-spatial objects derived from remotely sensed data. *International Journal of Remote Sensing*, 26, 2953-2974.

Zhan W., Chen Y., Zhou J., Li J., and Liu W., (2011). Sharpening thermal imageries: a generalized theoretical framework from an assimilation perspective. *IEEE Transactions on Geoscience and Remote Sensing*, 49 (2), 773-789.

Zhang X., Friedl M. A., Schaaf C. B., Strahler A. H., Hodges J. C. F., Gao F., Reed B. C., and Huete A. (2003), Monitoring vegetation phenology using MODIS. *Remote Sensing of Environment*, 84(3), 471-475.

ACKNOWLEDGEMENT

First of and foremost, I would like to express my deepest gratitude to my supervisor, Prof. Yasushi Yamaguchi, for his illuminating instruction, continuous encouragement and motivation throughout all my doctoral studies in Nagoya University. I greatly appreciate him offering me a free research environment where I can develop the study topic which I am interested in, His wide knowledge and creative way of thinking have been great value for me, and he also provided his facility and funding to support the whole process of my research and paper publishing. Besides the professional knowledge, I also learned about his kindness in communication and carefulness in work, which I believe will benefit me much in my future career.

Simultaneously, I would like to express my appreciation to Dr. Sasai and all of the members in the lab of earth environmental system for their help on my study and life, for meaningful suggestions and comments in each seminar, for the impressed atmosphere of hard studying and kind cooperation they created in this lab. Especially I would like to thank Mr. Yusheng Shi for his useful suggestions and kind help on my study and life. And I would like to thank Miss Anna Kato, Ms. Loan T. K. Ho, Mr. Tatsumi Uezato and Mr. Xiaoqiang Zhang for our stimulating group discussion. I would also like to thank Miss Fushi Kim for her kind help on addressing many issues of language barrier.

My heartfelt gratitude also goes to Prof. Jin Chen at Beijing Normal University, who gave me many instructive suggestions and advisements throughout my study. Also, I would like to thank the students in his lab for their help in the field investigation in Inner Mongolia in 2010 even though the data collected was not used in this thesis.

I also thank Prof. Nakamura and Prof. Tanikawa for their careful reviewing and valuable comments, which help to improve this thesis.

I would also like to thank Nagoya University Global COE Program (From Earth System Science to Basic and Clinical Environmental Studies) for providing me a wonderful experience of multi-discipline study. Thanks especially go to members in GCOE program including Prof. Masao Takano, Dr. Chen Liu, Dr. Hiromi Yamashita, Ms. Chuntao Wu and so on. My knowledge was largely expanded by working with them.

I also gratefully acknowledge Ministry of Education, Culture, Sports, Science and Technology (MEXT) for awarding me Government Scholarship, and GEO Grid of the Agency of Industrial Science and Technology for providing me the satellite data used in this thesis.

Thanks also go to all of my friends in Japan. With the memories of joy and help from them, I will never forget the great times we spent together in the last three years.

Finally, I would thank my beloved parents for their long-distance support and encouragement in every moment of my life. Whatever I achieved is only to make them happy and proud.

Xuehong Chen

July, 2012